Monthly Notices of the ROYAL ASTRONOMICAL SOCIETY

MNRAS **435,** 64–86 (2013)
Advance Access publication 2013 August 23

doi:10.1093/mnras/stt1261

The clustering of galaxies in the SDSS-III Baryon Oscillation Spectroscopic Survey: measuring $H(z)$ and $D_A(z)$ at $z = 0.57$ with clustering wedges

Eyal A. Kazin,[1,2]⋆ Ariel G. Sánchez,[3] Antonio J. Cuesta,[4] Florian Beutler,[5] Chia-Hsun Chuang,[6] Daniel J. Eisenstein,[7] Marc Manera,[8] Nikhil Padmanabhan,[4] Will J. Percival,[8] Francisco Prada,[6,9,10] Ashley J. Ross,[8] Hee-Jong Seo,[5] Jeremy Tinker,[11] Rita Tojeiro,[8] Xiaoying Xu,[12] J. Brinkmann,[13] Brownstein Joel,[14] Robert C. Nichol,[8] David J. Schlegel,[5] Donald P. Schneider[15,16] and Daniel Thomas[8]

[1]*Centre for Astrophysics & Supercomputing, Swinburne University of Technology, PO Box 218, Hawthorn VIC 3122, Australia*
[2]*ARC Centre of Excellence for All-sky Astrophysics (CAASTRO), 44 Rosehill Street, Redfern, NSW 2016, Australia*
[3]*Max-Planck-Institut für Extraterrestrische Physik, Giessenbachstraße, D-85748 Garching, Germany*
[4]*Department of Physics, Yale University, 260 Whitney Ave, New Haven, CT 06520, USA*
[5]*Lawrence Berkeley National Lab, 1 Cyclotron Rd, Berkeley, CA 94720, USA*
[6]*Instituto de Física Teórica, (UAM/CSIC), Universidad Autónoma de Madrid, Cantoblanco, E-28049 Madrid, Spain*
[7]*Harvard–Smithsonian Center for Astrophysics, 60 Garden St, Cambridge, MA 02138, USA*
[8]*Institute of Cosmology & Gravitation, University of Portsmouth, Dennis Sciama Building, Portsmouth PO1 3FX, UK*
[9]*Instituto de Astrofísica de Andalucía (CSIC), Glorieta de la Astronomía, E-18080 Granada, Spain*
[10]*Campus of International Excellence UAM+CSIC, Cantoblanco, E-28049 Madrid, Spain*
[11]*Center for Cosmology and Particle Physics, New York University, New York, NY 10003, USA*
[12]*Department of Physics, Carnegie Mellon University, 5000 Forbes Ave., Pittsburgh, PA 15213, USA*
[13]*Apache Point Observatory, 2001 Apache Point Rd, Sunspot, NM 88349, USA*
[14]*Department of Physics and Astronomy, University of Utah, 115 S 1400 E, Salt Lake City, UT 84112, USA*
[15]*Department of Astronomy and Astrophysics, The Pennsylvania State University, University Park, PA 16802, USA*
[16]*Institute for Gravitation and the Cosmos, The Pennsylvania State University, University Park, PA 16802, USA*

Accepted 2013 June 29. Received 2013 May 28; in original form 2013 March 2

ABSTRACT

We analyse the 2D correlation function of the Sloan Digital Sky Survey-III Baryon Oscillation Spectroscopic Survey (BOSS) CMASS sample of massive galaxies of the ninth data release to measure cosmic expansion H and the angular diameter distance D_A at a mean redshift of $\langle z\rangle = 0.57$. We apply, for the first time, a new correlation function technique called *clustering wedges* $\xi_{\Delta\mu}(s)$. Using a physically motivated model, the anisotropic baryonic acoustic feature in the galaxy sample is detected at a significance level of 4.7σ compared to a featureless model. The baryonic acoustic feature is used to obtain model-independent constraints $cz/H/r_s = 12.28 \pm 0.82$ (6.7 percent accuracy) and $D_A/r_s = 9.05 \pm 0.27$ (3.0 per cent) with a correlation coefficient of -0.5, where r_s is the sound horizon scale at the end of the baryonic drag era. We conduct thorough tests on the data and 600 simulated realizations, finding robustness of the results regardless of the details of the analysis method. Combining this with r_s constraints from the cosmic microwave background, we obtain $H(0.57) = 90.8 \pm 6.2\,\mathrm{km\,s^{-1}\,Mpc^{-1}}$ and $D_A(0.57) = 1386 \pm 45$ Mpc. We use simulations to forecast results of the final BOSS CMASS data set. We apply the reconstruction technique on the simulations demonstrating that the sharpening of the anisotropic baryonic acoustic feature should improve the detection as well as tighten constraints of H and D_A by $\sim$30 per cent on average.

Key words: cosmological parameters – distance scale – large-scale structure of Universe.

⋆E-mail: eyalkazin@gmail.com

1 INTRODUCTION

One of the most exciting recent observation is the acceleration of the expansion of the Universe since redshift $z = 1$ (Riess et al. 1998; Perlmutter et al. 1999). The origin of this phenomenon is thought to be an energy component with negative pressure (e.g. the so-called dark energy or a cosmological constant) or otherwise a break down of general relativity (GR; Einstein 1916) on cosmic scales. For an in-depth summary of the observed acceleration and its possible interpretations, see Weinberg et al. (2012).

One method of measuring geometry from a 3D map of cosmological objects is through a geometric technique called the Alcock–Paczynski test (Alcock & Paczynski 1979) along with a standard ruler known as the baryonic acoustic feature. Alcock & Paczynski (1979) demonstrated that by assuming an incorrect cosmology when converting observed redshifts z_{obs} to comoving distances χ, a spherical cosmological body will appear deformed due to geometrical distortions. In the context of galaxy maps, this would cause a coherent distortion of the apparent radial positions and an anisotropic signature in clustering probes. Reproducing an isotropic clustering signal would result in obtaining the true cosmology. The observable of this process is HD_{A}, where H is the expansion factor and D_{A} is the angular diameter distance. In practice, however, the observer must take into account another source of apparent clustering anisotropies due to redshift distortions, which arise because of contributions of line-of-sight peculiar velocities to redshift measurements (Kaiser 1987), making the line of sight a preferred direction. By accounting for both of these anisotropic patterns of geometric and dynamic distortions, HD_{A} may be measured. However, this degeneracy can be broken, and hence improved cosmological parameter constraints may be obtained, by applying the geometric correction technique on a standard ruler, such as the baryonic acoustic feature.

Early Universe plasma photon waves propagated at close to the speed of sound from overdense regions, came to a near halt at the era of decoupling of photons from baryons at $z_* \sim 1100$ at a characteristic comoving distance of $r_{\mathrm{s}} \sim 150$ Mpc from the originating overdensity. This process left a distinctive signature in cosmic microwave background (CMB) anisotropies and in the large-scale structure (LSS) of galaxies (Peebles & Yu 1970). Hu, Sugiyama & Silk (1997) review how the CMB anisotropies can be used to constrain fundamental cosmological parameters. Bassett & Hlozek (2010) review the baryonic acoustic signature in the clustering of matter and its usage as a standard ruler.

Following first baryonic acoustic feature measurements in the clustering of galaxies by Eisenstein et al. (2005) and Cole et al. (2005), two recent surveys, the WiggleZ Dark Energy Sky Survey (Drinkwater et al. 2010) and the Sloan Digital Sky Survey III (SDSS-III; York et al. 2000; Eisenstein et al. 2011) Baryon Oscillation Spectroscopic Survey (BOSS; Dawson et al. 2013), have reported detections of the baryonic acoustic feature at $z > 0.5$ (Blake et al. 2011b,d; Anderson et al. 2012; Sánchez et al. 2012) as well as the six degree field (6dF) Galaxy Survey (Jones et al. 2009) at $z < 0.2$ (Beutler et al. 2011). Busca et al. (2013) and Slosar et al. (2013) also detect the baryonic acoustic feature, for the first time, in the Lyman α forest of BOSS quasars between $2 < z < 3$.

The focus of most of these studies has been on the angle-averaged signal which constrains $(D_{\mathrm{A}}^2/H)^{1/3}/r_{\mathrm{s}}$, where r_{s} is the sound horizon at the end of the baryon drag era z_{d} (see Section 2).

The subject of this study is breaking the D_{A}^2/H degeneracy by using the Alcock–Paczynski effect through anisotropic clustering. This approach was first suggested by Hu & Haiman (2003) by using the 2D power spectrum $P(\boldsymbol{k})$. As pointed out in various studies, actual applications require distinguishing between anisotropic clustering effects caused from geometric distortions and those generated by redshift distortions. We discuss this issue in Section 2. A first simulated application was performed by Wagner, Müller & Steinmetz (2008) who used mock catalogues at $z = 1$ and 3 to demonstrate the usefulness of the technique. Shoji, Jeong & Komatsu (2009) argued that H and D_{A} information is encoded in the full 2D shape, and presented a generic algorithm that takes into account redshift distortions on all scales, assuming all non-linear effects are understood. First attempts to apply these techniques on 2D $P(\boldsymbol{k})$ and $\xi(\boldsymbol{s})$ clustering planes were performed by Okumura et al. (2008), Chuang & Wang (2012a) and Blake et al. (2011c).

Padmanabhan & White (2008) suggested decomposing the 2D correlation function into Legendre moments. They argue that the monopole (ξ_0 angle-averaged signal) and the quadrupole components (ξ_2, see equation 10) contain most of the relevant constraining information. Taruya, Saito & Nishimichi (2011) and Kazin, Sánchez & Blanton (2012) show that the hexadecapole term ξ_4 contains extra constraining power, which could be harnessed in the future with higher signal-to-noise ratio (S/N) than that currently available.

The advantage of analysing 1D projections over the 2D plane is the relative simplicity of building a stable covariance matrix.

The first analyses of the anisotropic baryonic acoustic feature using ξ_0 and ξ_2 have been performed on the SDSS-II luminous red galaxy sample ($z \sim 0.35$; Chuang & Wang 2012a,b; Xu et al. 2012) and the Data Release 9 (DR9)-CMASS sample tested here ($z \sim 0.57$; Reid et al. 2012).

We analyse, for the first time, an alternative 1D basis suggested by Kazin et al. (2012), called *clustering wedges* $\xi_{\Delta\mu}(s)$. Gaztañaga, Cabré & Hui (2009) focused on a narrow clustering cylinder $\xi(s_{||}, s_\perp < 5\ h^{-1}\mathrm{Mpc})$. In a subsequent analysis, Kazin et al. (2010) proposed using wider clustering wedges $\xi_{\Delta\mu}(s)$ to improve S/N of the measurements. Kazin et al. (2012) analysed the constraining power of H and D_{A} of $\xi_{\Delta\mu=0.5}(s)$ on mock catalogues. They concluded that these statistics should be comparable in performance to the multipoles (ξ_0, ξ_2) and provide a useful tool to test for systematics. The current study is the first analysis to perform such a thorough comparison on both data and mock galaxy catalogues.

Our analysis differs from the previous ones in a few other aspects. First, we compare results both before and after reconstruction. Reconstruction is a technique which corrects for the damping of the baryonic acoustic feature due to the large-scale coherent motions of galaxies. The baryonic acoustic feature is sharpened by calculating the displacement field and shifting galaxies to their near-original positions (Eisenstein et al. 2007b). Secondly, we follow a similar approach as in Xu et al. (2012), by focusing on $cz/H/r_{\mathrm{s}}$ and $D_{\mathrm{A}}/r_{\mathrm{s}}$ and marginalizing over shape information. One notable difference from Xu et al. (2012), however, is that they apply a linear approximation of the Alcock–Paczynski test, where we use the full non-linear equations. We compare both methods in Appendix B, and show that the linear approach underestimates the uncertainties of the obtained constraints. Finally, we compare between two independent theoretical ξ templates.

This study is part of a series of papers analysing the anisotropic clustering signal of the DR9-CMASS galaxy sample, containing 264 283 massive galaxies between $0.43 < z < 0.7$. Here, we measure H and D_{A} in a model-independent fashion through $\Delta\mu = 0.5$ clustering wedges. Anderson et al. (2013) uses 'consensus' values of clustering wedges and multipoles to infer cosmological implications.

Both of these studies focus on the information contained within the anisotropic baryonic acoustic feature. Two further studies analyse the information from the full shape of $\xi(\boldsymbol{s})$: Sánchez et al. (2013) use the $\xi_{\Delta\mu=0.5}$ and Chuang et al. (2013) focus on the multipoles $\xi_{0,2}$.

This study is constructed as follows: in Section 2 we explain in detail the geometric information encoded in redshift maps. In Section 3, we define the clustering wedges and in Section 4 we present the data and mock catalogues. In Section 5, we describe the method used in our analysis; Section 6 describes our results. We discuss the results in Section 7 and summarize in Section 8.

To avoid semantic confusion, we briefly explain here the terminology of the different spaces mentioned throughout the text. First, all analyses are based on two-point correlation functions, which we refer to as configuration space, as opposed to the Fourier domain called *k* space. Secondly, when referring to a space affected by redshift distortions, we call it redshift space and when there are none we refer to it as real space.

All the fiducial values calculated here are based on using the *WilkinsonMicrowaveAnisotropyProbe* 7 (*WMAP*7) flat Λ cold dark matter (ΛCDM) cosmology (Komatsu et al. 2011). To calculate comoving distances, we assume the matter density $\Omega_{\rm M} = 0.274$. Assuming $h = 0.7$ this yields fiducial values: $H^{\rm f} = 93.57\,{\rm km\,s^{-1}\,Mpc^{-1}}$, $D_{\rm A}^{\rm f} = 1359.6\,{\rm Mpc}$ at $z = 0.57$. Throughout, we also use derived unitless relationships $(cz/H/r_{\rm s})^{\rm f} = 11.94$, $(D_{\rm A}/r_{\rm s})^{\rm f} = 8.88$, where $r_{\rm s}^{\rm f} = 153.1$ Mpc (at $z_{\rm d}^{\rm f} = 1020$). For these we assume the baryon density $\Omega_{\rm b} h^2 = 0.0224$, radiation density $10^5\Omega_{\rm r} h^2 = 4.17$ and photon density of $10^5\Omega_\gamma h^2 = 2.47$.

2 COSMIC GEOMETRY FROM GALAXY MAPS

Although galaxy distributions in real space are assumed to be statistically isotropic, measured clustering signals from galaxies from redshift maps are anisotropic. This is a result of two physical effects that are at play when converting observed redshifts $z_{\rm obs}$ to comoving distances χ:

$$\chi(z_{\rm obs}) = c\int_0^{z_{\rm obs}} \frac{{\rm d}z}{H(z)}. \tag{1}$$

The first, which we refer to as redshift distortions, stems from the fact that $z_{\rm obs}$ is a degenerate combination of the cosmological flow and the radial component of the peculiar velocity. This results in anisotropic clustering components due to large-scale coherent flows (Kaiser 1987), and velocity dispersion effects within galaxy clusters. For a detailed introduction on dynamical redshift distortions see Hamilton (1998).

On large scales, these effects can be used to test for deviations from GR (Kaiser 1987; Linder 2008; see also Guzzo et al. 2007; Blake et al. 2011a; Beutler et al. 2012; Samushia, Percival & Raccanelli 2012; Samushia et al. 2013 for the most recent measurements). The observable in this test is $f\sigma_8$, where b is the linear tracer to matter density bias, $f \equiv {\rm d}D_1/{\rm d}\ln a$ is the rate of change of growth of structure, D_1 is the linear growth of structure, and σ_8 is the linear rms of density fluctuations averaged in spheres of radii 8 h^{-1}Mpc. This study focuses on a second more subtle effect which involves geometric distortions.

Comoving separations between two nearby points in space depend both on z and the observer angle between them Θ. Assuming the plane-parallel approximation between galaxy pairs, radial separations are defined as $s_{||} \equiv c\Delta z/H(z)$, where c is the speed of light, and transverse distances $s_\perp \equiv \Theta(1+z)D_{\rm A}$, where the proper (physical) angular diameter distance $D_{\rm A}$ is defined as

$$D_{\rm A} = \frac{1}{1+z}\frac{c}{H_0}\frac{1}{\sqrt{-\Omega_{\rm K}}}\sin\left(\sqrt{-\Omega_{\rm K}}\frac{\chi}{c/H_0}\right), \tag{2}$$

where $H_0 \equiv H(0)$ and $\Omega_{\rm K} = 1 - \sum_{\rm X}\Omega_{\rm X}$ is the representation of the curvature and $\Omega_{\rm X}$ are the energy densities of components X (matter, radiation, etc.).[1] Hence, assuming an incorrect cosmology in equation (1) would cause a spherical body (meaning $s_{||} = s_\perp$) to be deformed. For example, a lower $H(z)$ than the true one would cause an elongation along the line of sight due to an increased $s_{||}$, where a lower $D_{\rm A}(z)$ than the true value would cause a transverse squashing, because of a decrease of $s_\perp$. Therefore, by fixing the observables Θ and Δz, retrieving a spherical shape constrains the $HD_{\rm A}$ combination.

Various techniques have been suggested to measure $HD_{\rm A}$ through this Alcock–Paczynski test (AP henceforth; Alcock & Paczynski 1979; Phillipps 1994; Lavaux & Wandelt 2012). Here, we focus on clustering of galaxies, where line-of-sight clustering modes depend on $s_{||}$ $(1/H)$ and transverse modes on $s_\perp$ $(D_{\rm A})$, and hence the anisotropies due the AP effect.

It has been pointed out that the anisotropies from this geometric effect are degenerate with those from redshift effects (Ballinger, Peacock & Heavens 1996). Various studies, such as Blake et al. (2011c) and Reid et al. (2012), show the degeneracy between $HD_{\rm A}$ and $f\sigma_8$. In this study, we marginalize over the redshift distortion information and focus on the geometric distortions. In practice, when converting redshifts to comoving distances, the H_0 factors out trivially and thus we express comoving distance in units of h^{-1} Mpc, where $h \equiv H_0/(100\,{\rm km\,s^{-1}\,Mpc^{-1}})$. The rest of the parameters in $H(z)$ ($\Omega_{\rm X}$ and their equation of states $w_{\rm X}$) have more important, and potentially measurable, effects.

One way of overcoming these effects is to recalculate χ and then the clustering statistics for every point in the parameter spaces that we explore when determining cosmological constraints. However, that approach would be too expensive computationally; instead, we follow a simpler approach and compute our clustering statistics for a fixed fiducial cosmology and include the effect of this choice in our modelling of these measurements, as described below.

Although the baryonic acoustic feature comoving scale is fixed, the apparent position measured in the correlation function depends on $Hr_{\rm s}$ and $D_{\rm A}/r_{\rm s}$. As argued by Eisenstein et al. (2005), Anderson et al. (2013) show that the angle-averaged signal closely follows the $\left(D_{\rm A}^2/H\right)^{1/3}/r_{\rm s}$ degeneracy (see their fig. 8).

Padmanabhan & White (2008) show that analysis of the anisotropic signal adds $HD_{\rm A}$ information, and hence breaks the degeneracy. To break the degeneracy with $r_{\rm s}$ one needs to add additional information from the CMB anisotropies.

When relating $r_{\rm s}$ measured from the CMB to that in the LSS, one must take into account that these two definitions correspond to slightly different sound horizon radii (see equation 1 in Blake & Glazebrook 2003). Because the baryons have momentum at decoupling z_*, the baryonic acoustic signature in the distribution of matter is related to $r_{\rm s}(z_{\rm d}) > r_{\rm s}(z_*)$, where $z_{\rm d}$ is the epoch when the baryonic drag effectively ended (Eisenstein & Hu 1998). The baryonic acoustic signature in the CMB anisotropies corresponds to z_*. For current $r_{\rm s}(z_*)$ measurements, see Hinshaw et al. (2012), and for $r_{\rm s}(z_{\rm d})$ predictions from the CMB, see table 3 of Komatsu et al. (2009).

[1] Note that this is generic because $i\sin(ix) = -\sinh(x)$.

Conservation of the observer angle Θ means that true separations transverse to the line-of-sight component $s^t_\perp$ will be related to an apparent 'fiducial' component $s^f_\perp$ by[2]

$$s^t_\perp = s^f_\perp \cdot \alpha_\perp, \tag{3}$$

where

$$\alpha_\perp \equiv \frac{D^t_A}{D^f_A} \cdot \frac{r^f_s}{r^t_s}, \tag{4}$$

where the 'f' subscript indicates the fiducial cosmology when calculating $\chi(z)$ and 't' indicates the true cosmology.

Similarly, the true line-of-sight separation component is related to the fiducial by

$$s^t_{||} = s^f_{||} \cdot \alpha_{||}, \tag{5}$$

with

$$\alpha_{||} \equiv \frac{H^f}{H^t} \cdot \frac{r^f_s}{r^t_s}. \tag{6}$$

The sound horizon $r_s(z_d)$ terms appear due to the degeneracy with D_A and H, when applied to the baryonic acoustic feature as a standard ruler. Here, we quote the rescaling in the position of the peak of the ξ. The purely geometrical effect of changing the cosmology does not depend on $r_s(z_d)$. In Appendix A, we explain how we apply the AP test in practice through the mapping of ξ between these coordinates systems.

We also make use of an alternative representation of $\alpha_{||}$ and $\alpha_\perp$ through the isotropic dilation parameter α (Eisenstein et al. 2005) and the anisotropic warping parameter ϵ (Padmanabhan & White 2008):

$$\alpha \equiv \left(\frac{D_A}{D^f_A}\right)^{2/3} \left(\frac{H^f}{H}\right)^{1/3} \frac{r^f_s}{r_s} = \alpha_\perp^{2/3}\alpha_{||}^{1/3}; \tag{7}$$

$$1 + \epsilon = \left(\frac{D^f_A H^f}{D_A H}\right)^{1/3} = \left(\frac{\alpha_{||}}{\alpha_\perp}\right)^{1/3}. \tag{8}$$

3 CLUSTERING WEDGES

Assuming azimuthal statistical symmetry around the line of sight[3] the 3D correlation function $\xi(\boldsymbol{s})$ can be projected into 2D polar coordinates: the comoving separation s and the cosine of the angle from the line-of-sight μ, where the line-of-sight direction is $\mu = 1$.

The 2D plane of $\xi(\mu, s)$ can then be projected to *clustering wedges* $\Delta\mu$ as

$$\xi_{\Delta\mu}(\mu_{\min}, s) = \frac{1}{\Delta\mu} \int_{\mu_{\min}}^{\mu_{\min}+\Delta\mu} \xi(\mu, s)\, \mathrm{d}\mu. \tag{9}$$

For the purpose of this study, we focus on two clustering wedges of $\Delta\mu = 0.5$, which we call line-of-sight $\xi_{||}(s) \equiv \xi_{0.5}(\mu_{\min} = 0.5, s)$ and transverse $\xi_\perp(s) \equiv \xi_{0.5}(\mu_{\min} = 0, s)$. For consistency, we compare all results to the multipole statistics defined as

$$\xi_\ell(s) = \frac{2\ell + 1}{2} \int_{-1}^{+1} \xi(\mu, s)\mathcal{L}_\ell(\mu)\, \mathrm{d}\mu, \tag{10}$$

where $\mathcal{L}_\ell(x)$ are the standard Legendre polynomials.

The clustering wedges and multipoles are complementary bases of similar information. As shown by Kazin et al. (2012) up to order $\ell = 4$ they are related by

$$\xi_{||}(s) = \xi_0(s) + \frac{3}{8}\xi_2(s) - \frac{15}{128}\xi_4(s), \tag{11}$$

$$\xi_\perp(s) = \xi_0(s) - \frac{3}{8}\xi_2(s) + \frac{15}{128}\xi_4(s). \tag{12}$$

A useful relationship is the fact that the average of the $\Delta\mu = 0.5$ clustering wedges results in ξ_0.

In real space, where there are no anisotropies, all $\ell > 0$ components are nulled, and clustering wedges of any $\Delta\mu$ width correspond to the monopole signal.[4] The AP effect breaks this symmetry, causing $\ell > 0$ components due to geometric distortions.

4 DATA

We base our measurements of $cz/H/r_s$ and D_A/r_s on the large-scale anisotropic correlation function of the BOSS DR9-CMASS galaxy sample. Here, we give a brief description of the sample, and the calculated $\xi(\mu, s)$.

4.1 The DR9-CMASS galaxy sample

We use data from the SDSS-III BOSS survey (Eisenstein et al. 2011; Dawson et al. 2013). The galaxy targets for BOSS are divided into two samples, LOWZ and CMASS. These are selected on the basis of photometric observations carried out with a drift-scanning mosaic CCD camera (Gunn et al. 1998, 2006) on the Sloan Foundation telescope at the Apache Point observatory. Spectra of these galaxies are obtained using the double-armed BOSS spectrographs (Smee et al. 2013). Spectroscopic redshifts are then measured by means of the minimum-χ^2 template-fitting procedure described in Aihara et al. (2011), with templates and methods updated for BOSS data as described in Bolton et al. (2012).

Our analysis is based on the CMASS galaxy sample of SDSS DR9 (Ahn et al. 2012). This sample was designed to cover the redshift ranges $0.43 < z < 0.7$ down to a limiting stellar mass, resulting on a roughly constant number density of $n \simeq 3 \times 10^{-4}\, h^3\, \mathrm{Mpc}^{-3}$ (Eisenstein et al. 2011; Dawson et al. 2013; Padmanabhan et al., in preparation). This sample contains mostly central galaxies, with a $\sim$10 per cent satellite fraction (White et al. 2011; Nuza et al. 2013) and it is dominated by early-type galaxies, although it contains a significant fraction of massive spirals ($\sim$26 per cent; Masters et al. 2011).

Anderson et al. (2012) present a detailed description of the construction of a CMASS catalogue for LSS studies. We follow the procedure detailed there and refer the reader to that paper for more details.

4.2 PTHalo mock catalogues

Mock catalogues play a major role in the analysis and interpretation of LSS information, as they offer a useful tool to test for systematics and provide the means with which to estimate statistical errors. In this analysis, we use 600 PTHalo mock galaxy realizations to test our analysis pipeline and construct a covariance matrix of our measurements. Full details of the mock catalogues are given in Manera et al. (2013). Briefly, the mocks are based on dark matter second-order Lagrangian perturbation theory simulations, that were populated with mock galaxies within dark matter

[2] Here, we assume the plane-parallel approximation for each pair.

[3] The assumption of azimuthal statistical symmetry around the line of sight is true even with geometrical distortions.

[4] Homogeneity and isotropy are assumed here.

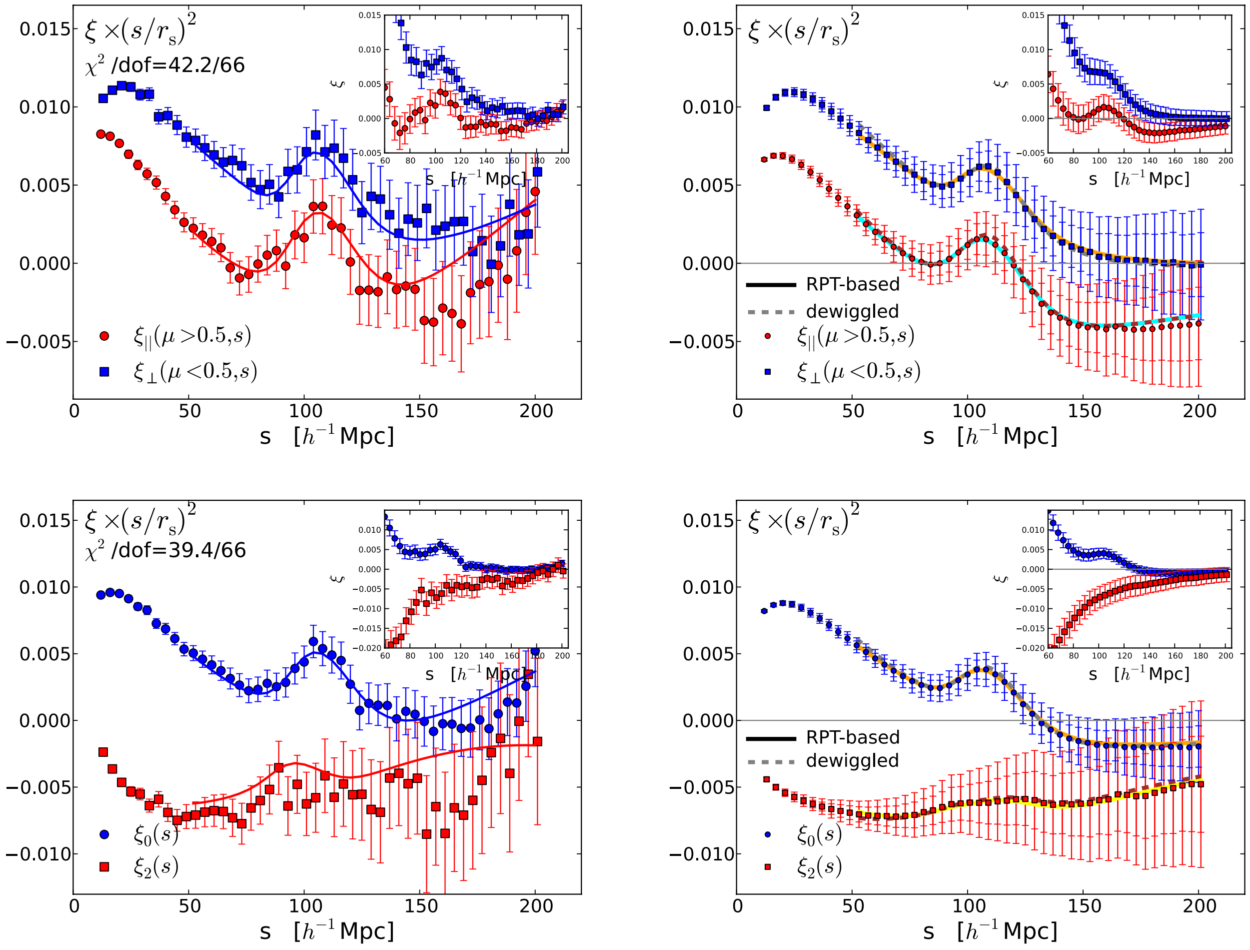

Figure 1. Top left: the pre-reconstruction DR9-CMASS $\langle z \rangle = 0.57$ clustering wedges are displayed multiplied by $(s/r_s)^2$ in the main plot, and without in the inset. Bottom left: the CMASS monopole and quadrupole. The solid lines in the left-hand panels are the renormalized perturbation theory (RPT)-based best-fitting models (see Section 5.2). The χ^2 and degrees of freedom are indicated. The uncertainty estimates are the square root of the diagonal elements of the covariance matrix. Right: the same statistics using the mean signal of 600 PTHalo mock realizations, where we display the same DR9 uncertainty bars, as well as those divided by $\sqrt{3}$ to illustrate the expected rms from the final BOSS-CMASS catalogue. The solid orange and yellow lines in the right-hand panels are the RPT-based templates, and the dashed grey and brown are the dewiggled templates. (For clarity the $\xi_\perp$ and ξ_2 data and templates are shifted by 1 h^{-1}Mpc.) The $\xi_{||}$ ($\mu > 0.5$ red circles) is clearly weaker than the $\xi_\perp$ ($\mu < 0.5$ blue squares), due to redshift distortions. In both clustering wedges, there is a clear signature of the baryonic acoustic feature.

haloes. The halo occupation distribution (Peacock & Smith 2000; Seljak 2000; Scoccimarro et al. 2001; Berlind & Weinberg 2002; Cooray & Sheth 2002) parameters are determined by comparing the correlation function to that of the data in the scale range of [30, 80] h^{-1}Mpc.

To match the selection function of the data, the mock data are split by the northern and southern CMASS angular geometry and galaxies were excluded to match the radial profile.

4.3 The anisotropic correlation function

To compute the correlation function, we use the Landy & Szalay (1993) estimator with an angular dependence

$$\xi(\mu, s) = \frac{DD(\mu, s) + RR(\mu, s) - 2DR(\mu, s)}{RR(\mu, s)}. \tag{13}$$

We calculate the normalized data–data pair counts in bins of evenly separated μ and s, $DD(\mu, s)$, and similarly for data–random pairs, DR, and random–random, RR, where for each pair $\mu = 1$ is defined as the direction in which a vector from the observer bisects $\boldsymbol{s}$. The μ values of each bin are the flat mean value. Our choice of binning is $\Delta\mu = 1/100$ and $\Delta s = 4$ h^{-1}Mpc.

To obtain the clustering wedges we use equation (9), where for $\xi_\perp(s)$ we use the μ range [0,0.5] and for $\xi_{||}(s)$ [0.5,1]. The resulting pre-reconstruction clustering wedges and multipoles are presented in top and bottom panels of Fig. 1, respectively. The line-of-sight wedge $\xi_{||}(\mu > 0.5, s)$ is clearly weaker than the transverse wedge $\xi_\perp(\mu < 0.5, s)$. This large difference in amplitudes on large scales is due to redshift distortions.

For comparison, in the right-hand panels of Fig. 1 we show the mock-mean signals, i.e. the mean $\xi_{\Delta\mu}$ and ξ_ℓ of 600 mock catalogues.

4.4 Reconstructing the baryonic acoustic feature

Eisenstein et al. (2007b) showed that large-scale coherent motions, which cause a damping of the baryonic acoustic feature, can be ameliorated by using the gravitational potential estimated from the large-scale galaxy distribution to predict the bulk flows, and undo their non-linear effect on the density field. First studies focusing

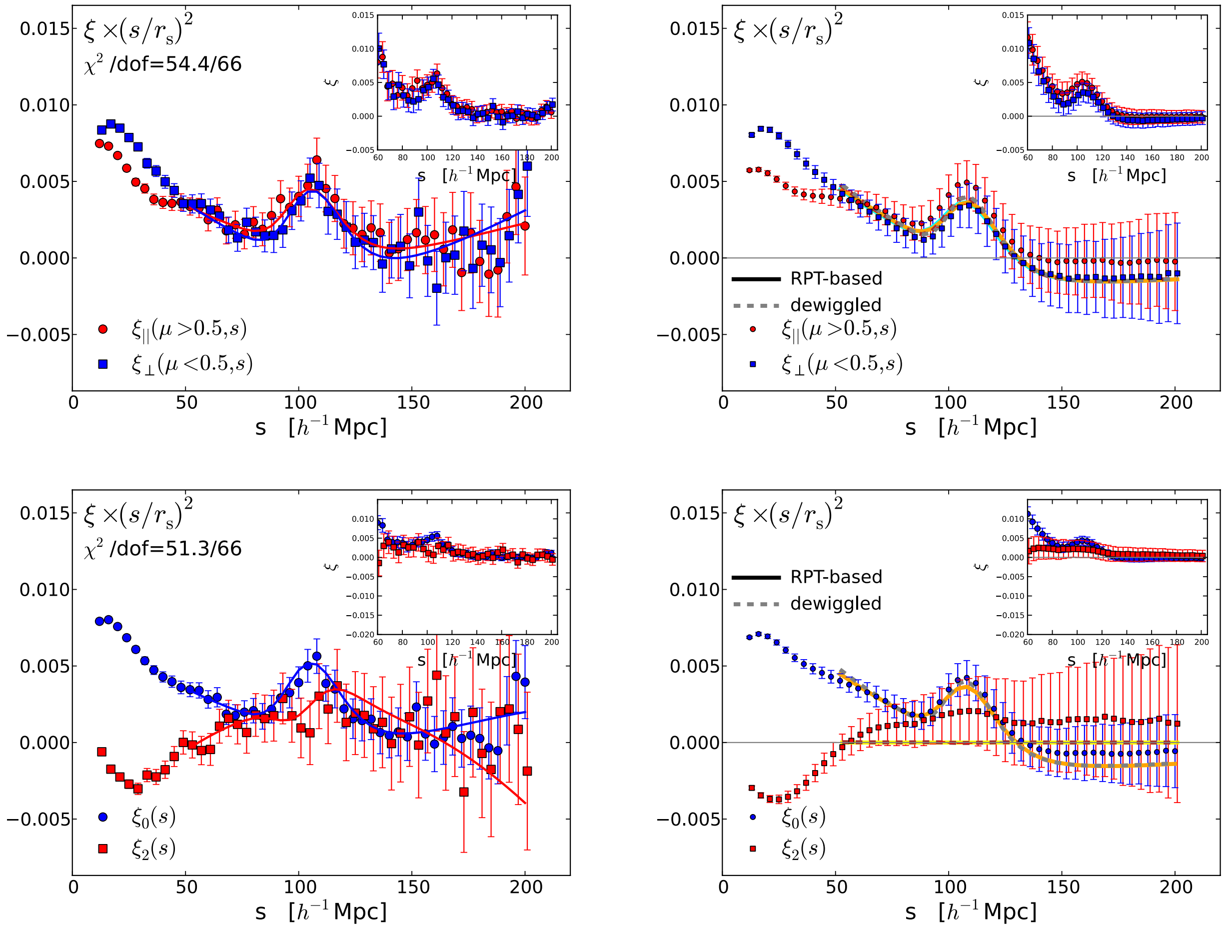

Figure 2. Top left: the post-reconstruction DR9-CMASS $\langle z \rangle = 0.57$ clustering wedges are displayed multiplied by $(s/r_s)^2$ in the main plot, and without in the inset. Bottom left: the CMASS monopole and quadrupole. The solid lines in the left-hand panels are the RPT-based best-fitting models (see Section 5.2). The χ^2 and degrees of freedom are indicated. The uncertainty estimates are the square root of the diagonal elements of the covariance matrix. Right: the same statistics using the mean signal of 600 PTHalo mock realizations. The solid orange and yellow lines in the right-hand panels are the RPT-based templates, and the dashed grey are the dewiggled templates. The RPT-based ξ_2 is set to zero, and that of the dewiggled template is small, as explained in Section 5.2.2. (For clarity the $\xi_\perp$ and ξ_2 data and templates are shifted by 1 h^{-1}Mpc.) The line-of-sight wedge ($\mu > 0.5$ red circles) is similar to the transverse wedge ($\mu < 0.5$ blue squares). This result shows that reconstruction substantially reduces effects of redshift distortions. In both clustering wedges there is a clear signature of the baryonic acoustic feature.

on periodic boxes have shown that this reconstruction technique sharpens the baryonic acoustic feature, and hence improves its usage as a standard ruler (Noh, White & Padmanabhan 2009; Padmanabhan, White & Cohn 2009; Seo et al. 2010; Mehta et al. 2011). We follow the procedure in Padmanabhan et al. (2012), which takes into account practical issues as edge effects by applying a Weiner filter (Hoffman & Ribak 1991; Zaroubi et al. 1995). We apply the reconstruction procedure on both the DR9-CMASS data, as well as on the mocks.

Fig. 2 displays the post-reconstruction results for $\xi_{||,\perp}(s)$ (top left) and the $\xi_{0,2}(s)$ (bottom left). We clearly see that the amplitudes of the clustering wedges are aligned at the scales of the baryonic acoustic feature and larger. This is due to the fact that reconstruction not only corrects for large-scale coherent motions, but also corrects, to a certain extent, for redshift distortions, as is seen by the near nullifying of the $\xi_2(s)$.

For comparison, in the right-hand panels of Fig. 2 we show results of the post-reconstruction mock-mean signal. We clearly see that the $\xi_2(s)$ reverses from negative at baryonic acoustic feature scales from the pre-reconstruction signal to positive. This change might be attributed to an overcompensation of the redshift distortions. In other words, throughout the reconstruction process, we estimate f to shift galaxies in the radial direction, with the aim to reduce the Kaiser effect. An overestimation could potentially put field galaxies a bit further away from high dense regions, and hence reverse the $\xi_2(s)$ signal, yielding a $\xi_\perp(s)$ that is slightly weaker than the $\xi_{||}(s)$. We are not concerned with this issue, because we do not expect redshift distortions to shift the position of the anisotropic baryonic acoustic feature.

In both clustering wedges, in pre- and post-reconstruction, there is a clear signature of the baryonic acoustic feature. We quantify the significance of the detection in Section 6.1.

5 ANALYSIS METHODOLOGY

5.1 Statistics used

When computing likelihoods of a model M with a variable parameter space Φ to fit data D, we calculate the χ^2:

$$\chi^2(\Phi) = \sum_{i,j} (M_i(\Phi) - D_i) C_{ij}^{-1} (M_j(\Phi) - D_j), \tag{14}$$

where i, j are the bins tested. The likelihood is then assumed to be Gaussian $L(\Phi) \propto \exp(-\frac{1}{2}\chi^2(\Phi))$.

Throughout this analysis, we run Monte Carlo Markov chains (MCMC) nominally for 9 or 10 parameters as described in Section 5.3. We quote the mode of the posterior as our *measurement* and half the 68 per cent CL region for the *uncertainty*, because these are well defined regardless of asymmetries in likelihood profiles.

5.1.1 Covariance matrix

We construct the covariance matrix C_{ij} from the $N_{\rm mocks} = 600$ mock catalogues. (For a description of the mocks used see Section 4.2.) The $\xi_{||,\perp}$ signals are not independent but have significant cross-correlations. To take these correlations into account, when constructing the C_{ij}, we treat the mocks signals in an array of the form $\xi_{[2s]} = [\xi_{||}, \xi_{\perp}]$, meaning a 1D array with twice the length of the separation range of analysis. When analysing the multipoles we apply a similar convention $\xi_{[2s]} = [\xi_0, \xi_2]$. We then construct a covariance matrix of $\xi_{[2s]}$ defined as

$$C_{ij} = \frac{1}{N_{\rm mocks} - 1} \sum_{m=1}^{N_{\rm mocks}} \left(\overline{\xi}_{[2s]i} - \xi^m_{[2s]i}\right)\left(\overline{\xi}_{[2s]j} - \xi^m_{[2s]j}\right). \quad (15)$$

Fig. 3 shows the correlation matrix $C_{i,j}/\sqrt{C_{i,i}C_{j,j}}$ of $\xi_{||,\perp}$ pre- and post-reconstruction. The $\xi_{\perp}$ quartile has slightly larger (normalized) off-diagonal terms than in the $\xi_{||}$ quartile, demonstrated by the less steep gradient. There are also non-trivial positive and negative covariance cross-terms between the $\xi_{\perp}$ and $\xi_{||}$. In the reconstructed $C_{i,j}$, we notice a sharper gradient, and a shallower negative region, indicating less dominance of the off-diagonal terms. This means that the reconstruction procedure reduces the covariance between the data points. Examining $C_{i,j}$ of the $\xi_{0,2}$ we find similar trends.

Fig. 4 displays the square root of the diagonal elements. It is clear that pre-reconstruction the scatter in the two clustering wedges is slightly different, where post-reconstruction they are similar, and less than that of pre-reconstruction. We clearly see that ξ_0 yields the lowest scatter of all the ξ statistics, and ξ_2 the highest, both pre- and post-reconstruction.

To correct for the bias due to the finite number of realizations used to estimate the covariance matrix and avoid underestimation of the parameter constraining region, after inverting the matrix to $C^{-1}_{\rm original}$, we multiply it by the correction factors (Anderson 2003; Hartlap, Simon & Schneider 2007):

$$C^{-1} = C^{-1}_{\rm original} \cdot \frac{(N_{\rm mocks} - N_{\rm bins} - 2)}{(N_{\rm mocks} - 1)}. \quad (16)$$

In our analysis $N_{\rm mocks} = 600$, $N_{\rm bins} = 76$ (2×38) (when analysing region [50,200] h^{-1}Mpc), yielding a factor of 0.87.

5.2 Non-linear ξ templates

The modelling is split into two parts: inclusion of redshift distortions and modelling for non-linearities. Here we describe the former, and later consider two procedures for defining non-linearities.

Once the non-linear $P_{\rm NL}$ is defined (see Section 5.2.1), redshift distortions are added such that the non-linear z-space power spectrum is

$$P^{\rm S}_{\rm NL}(k, \mu_k) = \frac{1}{(1 + (kf\sigma_{\rm V}\mu_k)^2)^2}\left(1 + \beta\mu_k^2\right)^2 P_{\rm NL}, \quad (17)$$

where $\beta \equiv f/b$.

Although the velocity dispersion parameter $\sigma_{\rm V}$ appears to be an unresolved subject of investigation (Taruya et al. 2009), we find that applying it in the above Lorentzian format yields a good agreement with the mock-mean signals $\xi_{||,\perp}$ and $\xi_{0,2}$ down to $s > 50\ h^{-1}$Mpc. We find the Lorentzian format, which corresponds to an exponential pairwise velocity distribution (Park et al. 1994; Cole, Fisher & Weinberg 1995), is preferred over the popular Gaussian.

The conversion to configuration space is accomplished by means of equations 4.8 and 4.17 in Taruya et al. (2009). As described in Appendix A, we apply this calculation once to obtain the ξ_0, ξ_2 templates, which are stored during the MCMC calculations. This approach means that we fix the parameters f, β, $\sigma_{\rm V}$ constant, and allow for their effective changes through the $a_{0\ \rm stat}$ and $A(s)$ shape parameters, as described in Sections 5.3.1 and 6.3.3. The values assumed for these parameters are summarized in Table 1.

5.2.1 Non-linear $P(k)$

We use two anisotropic templates. The primary focus is on a physically motivated model based on RPT, which takes into account first-order corrections of k-mode coupling. Throughout this study, we compare performance of this template to one that describes the

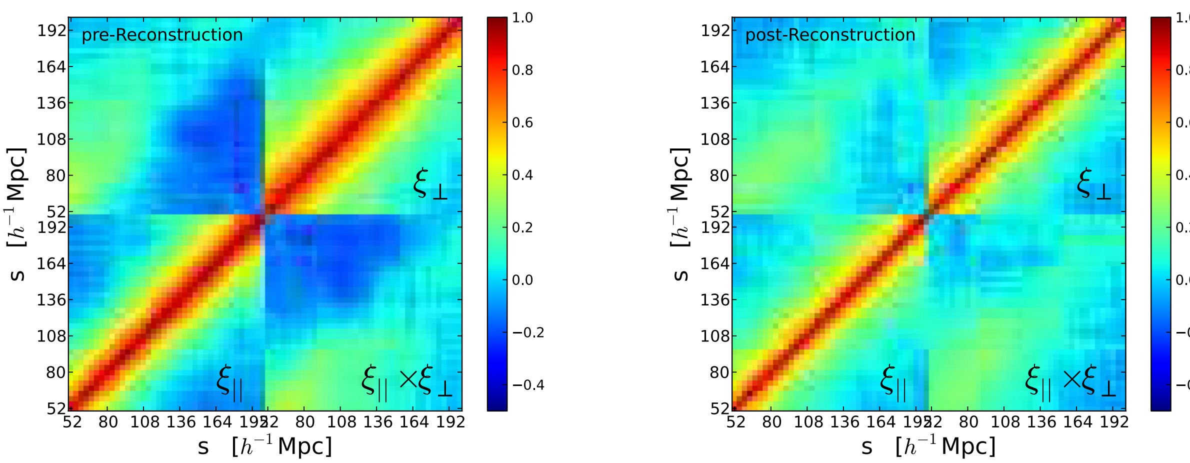

Figure 3. We use a suite of 600 PTHalo pre-reconstruction mock catalogues (left) and post-reconstruction (right) to construct the covariance matrix of the clustering wedges, displayed here in correlation matrix form $C_{i,j}/\sqrt{C_{i,i}C_{j,j}}$. The bottom-left quadrant is that of $\xi_{||}$, the top-right quadrant is that of $\xi_{\perp}$. The other quadrants, which are mirrored, are the cross-correlation between the bins of $\xi_{||}$ and $\xi_{\perp}$.

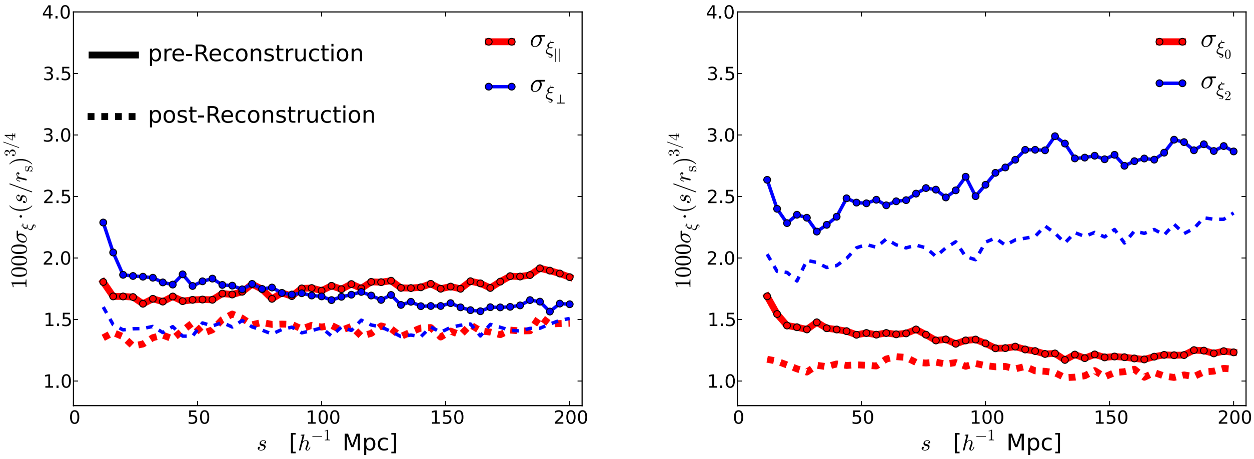

Figure 4. The $\sqrt{C_{ii}}$ values constructed from the pre- (solid) and post-reconstruction (dashed) mocks. Left-hand plot: results of the clustering wedges $\xi_{||}$ (thick red), $\xi_{\perp}$ (thin blue). Right-hand plot: similar for the ξ_0 (thick red), ξ_2 (thin blue). Reconstruction substantially reduces the covariance in these measurements.

Table 1. Non-linear anisotropic ξ templates.

Template name	Base equation	Fixed parameter values	Comment
$\xi^{\mathrm{RPT-based}}$ pre-rec	(18)	$k_{\mathrm{NL}} = 0.19\,h\,\mathrm{Mpc}^{-1}$, $A_{\mathrm{MC}} = 2.44$, $\sigma_{\mathrm{V}} = 5.26\,h^{-1}$Mpc	
$\xi^{\mathrm{RPT-based}}$ post-rec	(18)	$k_{\mathrm{NL}} = 0.50\,h\,\mathrm{Mpc}^{-1}$, $A_{\mathrm{MC}} = 2.44$, $\sigma_{\mathrm{V}} = 0\,h^{-1}$Mpc	$\xi_2 = 0$
$\xi^{\mathrm{dewiggled}}$ pre-rec	(20)	$\Sigma_{\|\|} = 11\,h^{-1}$Mpc, $\Sigma_{\perp} = 6\,h^{-1}$Mpc, $\sigma_{\mathrm{V}} = 1\,h^{-1}$Mpc	
$\xi^{\mathrm{dewiggled}}$ post-rec	(20)	$\Sigma_{\|\|} = \Sigma_{\perp} = 3\,h^{-1}$Mpc, $\sigma_{\mathrm{V}} = 1\,h^{-1}$Mpc	$\xi_2 \neq 0$ but small

Notes. The RPT-based templates are shown in Figs 1 (pre-rec; also shown in fig. 4 of Sánchez et al. 2013) and 2 (post-rec).
The dewiggled templates are shown in Figs 1 and 2 as well as fig. 1 of Anderson et al. (2013).
After the base equation is calculated, equation (17) includes redshift distortions (post-rec assumes $\beta = 0$).

effect of non-linearities in the baryonic acoustic feature through the 'dewiggling' procedure. Both templates assume an exponential damping of the baryonic acoustic feature due to large-scale coherent motions, where in RPT-based this is assumed to be isotropic and in dewiggled anisotropic.

For the RPT-based template we write

$$P_{\mathrm{RPT}}(k) = P_{\mathrm{Linear}}(k)\exp\left(-\left(\frac{k}{k_{\mathrm{NL}}}\right)^2\right) + A_{\mathrm{MC}}P_{1\mathrm{loop}}(k), \quad (18)$$

where

$$P_{1\mathrm{loop}}(k) = \frac{1}{4\pi^3}\int d\boldsymbol{q}|F_2(\boldsymbol{k}-\boldsymbol{q},\boldsymbol{q})|^2 P_{\mathrm{Linear}}(|\boldsymbol{k}-\boldsymbol{q}|)P_{\mathrm{Linear}}(\boldsymbol{q}). \quad (19)$$

The mode coupling term F_2 is given by equation (45) in Bernardeau et al. (2002). Pre-reconstruction we fix $k_{\mathrm{NL}} = 0.19\,h\,\mathrm{Mpc}^{-1}$, which causes damping of the baryonic acoustic feature, and $A_{\mathrm{MC}} = 2.44$ which takes into account mode coupling. These values are determined by analysing the mean signal of the mocks whilst fixing $cz/H/r_s$ and D_A/r_s to the true values (and not using shape parameters). See section 3 of Sánchez et al. (2013) for a thorough discussion of the template and a summary of earlier investigations (e.g. Crocce & Scoccimarro 2008; Sánchez, Baugh & Angulo 2008).

We compare the results obtained by means of the RPT-based model to a popular model denoted as dewiggled, which also includes a Gaussian damping of the baryonic acoustic feature:

$$P_{\mathrm{dewiggled}}(k,\mu_k) = \left(P_{\mathrm{Linear}} - P_{\mathrm{NoWiggle}}\right)\cdot\mathcal{D}(k,\mu_k) + P_{\mathrm{NoWiggle}}, \quad (20)$$

where the anisotropic damping is defined by

$$\mathcal{D}(k,\mu_k) \equiv \exp\left[-\frac{1}{2}k^2\left(\mu_k^2\Sigma_{||}^2 + \left(1-\mu_k^2\right)\Sigma_{\perp}^2\right)\right]. \quad (21)$$

The $P_{\mathrm{NoWiggle}}(k)$ is the no-wiggle model given in Eisenstein & Hu (1998). Here, we use values $\Sigma_{\perp}$, $\Sigma_{||} = 6$, $11\,h^{-1}$Mpc for the pre-reconstruction case, and $\Sigma_{||} = \Sigma_{\perp} = 3\ h^{-1}$Mpc for post-reconstruction. The values are chosen as those that best fit the mock-mean signal. For further discussion of testing these parameter values and comparisons the reader is referred to Section 4.3 in Anderson et al. (2013). For a thorough description of the anisotropic dewiggled model, the reader is referred to Eisenstein, Seo & White (2007a) and Xu et al. (2012).

The pre-reconstruction RPT-based templates and the dewiggled templates used are plotted in the right-hand panels of Fig. 1. These are compared with the mock-mean signal of 600 realizations. In addition to the DR9 uncertainties, we also show them divided by $\sqrt{3}$ to give an approximate estimation of the expected rms of the ξ from the final BOSS-CMASS volume, which should be three times the size of DR9-CMASS.

We see that both templates (solid – RPT-based; dashed – dewiggled) are similar and trace the mock mean well. We see a slight indication that the RPT-based template traces $\xi_{||}$ slightly better than the dewiggled, where the dewiggled template traces $\xi_{\perp}$ moderately better. As these differences are much smaller than the expected rms from one DR9 volume, we consider that a thorough comparison of the templates is beyond the scope of this study, and defer it for future analysis. Our focus here is comparing results of the templates used in Sánchez et al. (2013) (RPT-based) and Anderson et al. (2013)

(dewiggled). We refer the reader to these studies for more detailed explanations of construction of the templates.

5.2.2 Post-reconstruction templates

Equation (17) is used for both the RPT-based and dewiggled templates pre-reconstruction. Post-reconstruction templates are described in this section.

Assuming that the reconstruction procedure works correctly, one expects, in addition to the sharpening of the baryonic acoustic feature, a correction for redshift distortions, yielding an isotropic $\xi(s)$. We apply this approach in the RPT-based modelling. Due to the sharpening of the baryonic acoustic feature, we set $k_{\rm NL} = 0.50\,h\,{\rm Mpc}^{-1}$, which effectively yields the linear ξ. The isotropy in the post-reconstruction template is introduced by setting $\sigma_{\rm V}$, $\beta = 0$ and hence $\xi_2 = 0$.

Because the reconstructed field is not linear, the choice of the mode coupling term in the RPT-based template is not obvious. We test the mock realizations for various values of $A_{\rm MC}$ for the resulting $cz/H/r_{\rm s}$ and $D_{\rm A}/r_{\rm s}$ values. We find that setting $A_{\rm MC}$ to zero, yields a 0.7–1 per cent bias in $cz/H/r_{\rm s}$. For this reason, we fix $A_{\rm MC}$ to the same 2.44 value used in the pre-reconstruction template, which produces lower bias (<0.5 per cent see Tables 2 and C1).

For the dewiggled post-reconstruction template we assume an isotropic $P_{\rm NL}$ model, but do include $\sigma_{\rm V} = 1\ h^{-1}$Mpc contributions, which are small at the baryonic acoustic feature scale. This is the same template used in the analysis of Anderson et al. (2013). The reader is referred to that paper for a detailed description of choice of parameter values.

The post-reconstruction RPT-based templates and the dewiggled templates used are plotted in the right-hand panels of Fig. 2 (similar notation as in Fig. 1). These are compared with the mock-mean signal of 600 realizations, where the uncertainties are square root of the diagonal elements of C_{ij}.

Comparing the post-reconstruction clustering wedges templates to the mock data, we clearly see an amplitude disagreement indicating that the reconstruction procedure, as applied on the PTHalos, yields a systematic effect in ξ_2, which reverses sign at scales of the baryonic acoustic feature, suggesting that there might be an over-compensation of the Kaiser effect. We are not concerned by this

Table 2. Mock DR9 PTHalo results.

ξ (No. of realizations)	$\alpha_{\|\|}$ [a]	$\Delta\alpha_{\|\|}/\alpha_{\|\|}$ [b]	$\alpha_{\perp}$ [a]	$\Delta\alpha_{\perp}/\alpha_{\perp}$ [b]
Full sample, no priors:				
RPT-based wedges pre-rec (600)	0.970 ± 0.188	0.132 ± 0.075	1.006 ± 0.087	0.048 ± 0.061
RPT-based wedges post-rec (600)	0.997 ± 0.101	0.068 ± 0.065	1.000 ± 0.042	0.034 ± 0.033
RPT-based multipoles pre-rec (600)	0.986 ± 0.194	0.102 ± 0.076	1.001 ± 0.082	0.050 ± 0.053
RPT-based multipoles post-rec (600)	0.992 ± 0.176	0.077 ± 0.083	1.002 ± 0.052	0.037 ± 0.024
Dewiggled wedges pre-rec (600)	0.983 ± 0.190	0.129 ± 0.075	1.014 ± 0.086	0.047 ± 0.060
Dewiggled wedges post-rec (600)	0.999 ± 0.106	0.065 ± 0.067	1.002 ± 0.047	0.033 ± 0.036
Dewiggled multipoles pre-rec (600)	0.990 ± 0.183	0.100 ± 0.072	1.008 ± 0.086	0.049 ± 0.047
Dewiggled multipoles post-rec (600)	1.002 ± 0.134	0.056 ± 0.077	1.000 ± 0.045	0.030 ± 0.025
Full sample, $\|\epsilon < 0.15\|$:				
RPT-based wedges pre-rec (600)	0.982 ± 0.114	0.098 ± 0.049	1.002 ± 0.050	0.044 ± 0.034
RPT-based wedges post-rec (600)	0.998 ± 0.067	0.064 ± 0.038	0.999 ± 0.038	0.033 ± 0.020
$\geq 3\sigma$ subsample, no priors:				
RPT-based wedges pre-rec (462)	0.983 ± 0.146	0.103 ± 0.065	1.003 ± 0.064	0.042 ± 0.044
RPT-based wedges post-rec (462)	0.997 ± 0.086	0.061 ± 0.061	1.000 ± 0.034	0.032 ± 0.026
$\geq 4.0\sigma$ subsample, no priors:				
RPT-based wedges pre-rec (208)	0.990 ± 0.111	0.074 ± 0.054	1.001 ± 0.043	0.034 ± 0.027
RPT-based wedges post-rec (208)	0.996 ± 0.079	0.053 ± 0.051	0.999 ± 0.030	0.028 ± 0.020
$\geq 4.5\sigma$ subsample, no priors:				
RPT-based wedges pre-rec (104)	0.992 ± 0.099	0.065 ± 0.050	1.000 ± 0.035	0.031 ± 0.021
RPT-based wedges post-rec (104)	0.999 ± 0.045	0.052 ± 0.040	0.997 ± 0.024	0.028 ± 0.009
$\geq 3\sigma$ subsample, $\|\epsilon < 0.15\|$:				
RPT-based wedges pre-rec (462)	0.988 ± 0.102	0.089 ± 0.042	1.001 ± 0.048	0.040 ± 0.023
RPT-based wedges post-rec (462)	0.997 ± 0.061	0.059 ± 0.035	0.999 ± 0.031	0.031 ± 0.014
$\geq 3\sigma$ subsample, $\|\epsilon < 0.15\|$, $\|1 - {\rm mode}\| < 0.14$:				
RPT-based wedges pre-rec (394)	0.996 ± 0.060	0.087 ± 0.035	1.000 ± 0.037	0.040 ± 0.021
RPT-based wedges post-rec (450)	0.998 ± 0.046	0.059 ± 0.032	0.999 ± 0.029	0.031 ± 0.014
RPT-based multipoles pre-rec (374)	0.999 ± 0.061	0.079 ± 0.030	0.997 ± 0.038	0.044 ± 0.011
RPT-based multipoles post-rec (434)	1.001 ± 0.047	0.062 ± 0.030	0.998 ± 0.031	0.033 ± 0.011
Dewiggled wedges pre-rec (392)	1.003 ± 0.063	0.087 ± 0.036	1.009 ± 0.038	0.039 ± 0.019
Dewiggled wedges post-rec (445)	1.003 ± 0.047	0.056 ± 0.034	1.000 ± 0.031	0.030 ± 0.016
Dewiggled multipoles pre-rec (371)	1.003 ± 0.061	0.077 ± 0.030	1.006 ± 0.037	0.042 ± 0.019
Dewiggled multipoles post-rec (434)	1.006 ± 0.043	0.051 ± 0.033	0.999 ± 0.028	0.028 ± 0.007

[a]The $\alpha_{||}$ and $\alpha_{\perp}$ columns show the median and rms of the modes.
[b]The $\Delta\alpha_{||}/\alpha_{||}$ and $\Delta\alpha_{\perp}/\alpha_{\perp}$ columns show the median and rms of the fractional uncertainties.

fact, as we are interested in the peak positions to extract $cz/H/r_s$ and D_A/r_s, and not β. When using each of the templates, linear and non-linear systematics of the reconstruction procedure are corrected by the shape parameters as described in Section 5.3.1. In Section 6.2, we demonstrate that for the RPT-based model the post-reconstruction results are essentially unbiased.

5.3 The model tested

In this study, we focus on the geometric information $cz/H/r_s$ and D_A/r_s contained in ξ in a model-independent fashion. This is done by focusing on the information contained in the anisotropic baryonic acoustic feature, and hence marginalize over the shape effects, in a similar approach to that used in Xu et al. (2012, 2013) and Anderson et al. (2012).

For each statistic analysed we define a model based on a template using the following prescription:

$$\xi^{\rm model}_{\rm stat}(s_{\rm f}) = a_{0\ \rm stat} \cdot \xi^{\rm AP\ template}_{\rm stat}(s_{\rm f}) + A_{\rm stat}(s_{\rm f}), \tag{22}$$

where ($\xi_{\rm stat} = \xi_{||}, \xi_{\perp}, \xi_0$ or ξ_2). The $cz/H/r_s$ and D_A/r_s parameters are varied within $\xi^{\rm AP\ template}_{\rm stat}$ by application of the non-linear AP effect, as described in Section 2 and Appendix A. In Appendix B, we also compare the non-linear to the linear AP shift and conclude that for DR9-CMASS the linear method underestimates constraints by $\sigma^{\rm linear}_{\rm X}/\sigma^{\rm non-linear}_{\rm X} \sim 0.8$, where $\sigma^{\rm method}_{\rm X}$ is half of the 1D marginalized 68 per cent CL region of X=H, D_A.[5]

5.3.1 *The shape parameters*

As indicated in equation (22), each statistic 'stat' is multiplied by its own independent amplitude factor $a_{0\ \rm stat}$. These factors take into account effective variations of the linear σ_8, galaxy-to-matter linear bias, and the effective linear Kaiser boost. Since we marginalize over the two $a_{0\ \rm stat}$ factors independently we disregard all β information which is encoded in the amplitude difference in the pre-reconstruction $\xi_{\Delta\mu}$, as well other linear amplitude information. To take into account possible contributions of non-linear bias effects, non-linear redshift-distortions effects, as well as shape effects of the reconstruction procedure we marginalize over $A_{\rm stat}(s)$ terms as follows.

For each clustering wedge $\xi_{||,\perp}$ model, we add three additional non-linear parameters according to

$$A_{||}(s) = \frac{a_{1\ ||}}{s^2} + \frac{a_{2\ ||}}{s} + a_{3\ ||}, \tag{23}$$

$$A_{\perp}(s) = \frac{a_{1\ \perp}}{s^2} + \frac{a_{2\ \perp}}{s} + a_{3\ \perp}. \tag{24}$$

When testing for the $\xi_{0,2}$ we apply a similar approach. These $A(s)$ terms are applied to the model only after the original template is shifted by the AP mapping. Hence, the parameter space used contains 10 parameters:

$$\Phi_{10} = [cz/H/r_s, D_A/r_s, \mathcal{S}], \tag{25}$$

where

$$\mathcal{S} = [a_{0\ \rm stat1}, a_{1\ \rm stat1}, a_{2\ \rm stat1}, a_{3\ \rm stat1}, \\ a_{0\ \rm stat2}, a_{1\ \rm stat2}, a_{2\ \rm stat2}, a_{3\ \rm stat2}], \tag{26}$$

where $a_{i\ {\rm stat}j}$ is the ith shape parameter for the jth ξ-statistic, as described in equations (23) and (24).

In our analysis we find, however, that $a_{0\ \xi_2}$ is not well constrained both pre- and post-reconstruction (this is not the case for the rest of $a_{0\ \rm stat}$). We decide to fix this parameter, and hence are left with a nine parameter space Φ_9, when analysing $\xi_{[0,2]}$. In Appendix C, we verify that the results obtained with $\xi_{0,2}$ using Φ_9 yield similar results (modes and uncertainties) to those obtained with $\xi_{\Delta\mu}$ using Φ_{10} both pre- and post-reconstruction. In Section 6.3.3, we describe degeneracies of the shape parameters with $cz/H/r_s$ and D_A/r_s constraints.

5.3.2 *Priors*

We limit $\alpha_{\perp}$ and $\alpha_{||}$ each to the region [0.5,1.5]. As suggested by Xu et al. (2012), we test the effect of applying a Gaussian prior on the warping parameter ϵ. We also examine applying a flat prior on ϵ.

For most of this analysis, we do not use these priors, but we do examine using various ϵ prior values, and report a few results with a weak flat prior $|\epsilon| \leq 0.15$, which is motivated by current observational cosmology. We test cosmologies on *WMAP*7 data by varying Ω_K and time dependent $w_{\rm DE}$ and find that $|\epsilon > 0.07|$ is highly disfavoured. As shown below, the CMASS data, both pre- and post-reconstruction, show clear preference of small epsilon.

6 RESULTS

In this section, we determine the significance with which the DR9-CMASS anisotropic baryonic acoustic feature is detected, and compare this to simulated realizations. We later describe the measurements of $cz/H/r_s$ and D_A/r_s.

6.1 Significance of the detection of the anisotropic baryonic acoustic feature

We generalize the standard technique of determining the significance of the detection of the baryonic acoustic feature to the 2D anisotropic case by usage of the clustering wedges, and apply this to the DR9-CMASS and the 600 mock realizations.

The method involves comparing the lowest χ^2 result of a chosen physical model to a no-wiggle model. For a no-wiggle model, we use the Eisenstein & Hu (1998) formalism (see their section 4.2), and derive monopole and quadrupole components using equation (10).

Using this approach as a template, we run the same modelling and AP mapping (equation 22) with the same parameter space Φ_{10} as the physically motivated templates. In the procedure, we do not attempt to analyse the clustering wedges separately from each other, i.e. we do not attempt to quantify significance of detection of the baryonic acoustic feature only in $\xi_{||}$ or $\xi_{\perp}$. Instead, we quantify the significance of the detection of the anisotropic baryonic acoustic feature in the $\xi(\boldsymbol{s})$ by using both $\xi_{\Delta\mu}$. This is due to the covariance between the clustering wedges, as well as the strong correlation between $\alpha_{||}$ and $\alpha_{\perp}$. All the following results are similar when using the RPT-based or the dewiggled templates.

We apply this procedure on both the CMASS and the mock catalogues. The results are summarized in Fig. 5, where the left-hand panels correspond to pre-, and the right to post-reconstruction. The top two panels correspond to the CMASS $\Delta\chi^2 \equiv \chi^2_{\rm ref} - \chi^2$ results as a function of the marginalized $\alpha_{||}$ and $\alpha_{\perp}$. The thick blue lines

[5] Results from tests on the DR9-CMASS pre-reconstructed $\xi_{0,2}$.

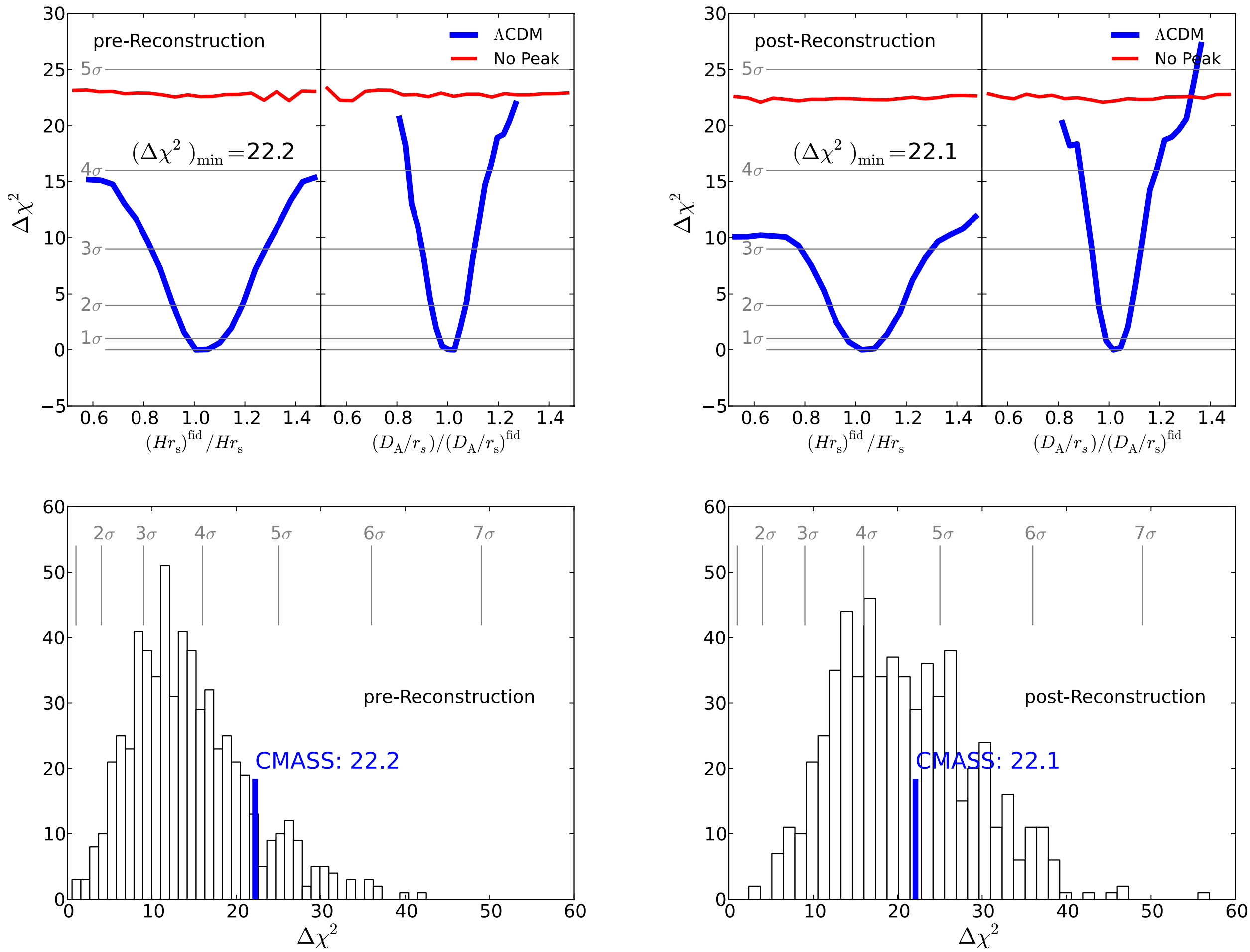

Figure 5. In the top plots, we examine the significance of the detection of the anisotropic baryonic acoustic feature in the CMASS clustering wedges by comparing χ^2 results of two templates: a physical ΛCDM template (thick blue) and one with no baryonic peak (thin red). In each panel in the plots, we display the minimum χ^2 surface for the marginalized $\alpha_{||}$ (left) and $\alpha_\perp$ (right). The reference χ^2 from which each binned result is compared to is that of the best fit of the ΛCDM model. The left-hand plots correspond to the data pre-reconstruction and the right to post-reconstruction. In CMASS, we find the significance of the detection of the anisotropic baryonic acoustic feature to be $\sqrt{\Delta\chi^2_{\rm min}} = 4.7\sigma$ for both the pre- and post-reconstruction cases. In the bottom plots, we run the same procedure on 600 mock catalogues and present the histogram of the distribution while indicating the CMASS result. The mock results show that reconstruction yields a clear expected improvement of significance of detection.

show the minimum χ^2 surface of the RPT-based model compared to its minimum $\chi^2_{\rm ref}$. The thin red line corresponds to the no-wiggle (no-peak) χ^2 surface minimum model compared with $\chi^2_{\rm ref}$. The bottom two panels are histogram results of the mock realizations, where the CMASS results are indicated with the thick vertical line. No priors on ϵ have been applied.

The pre-reconstruction CMASS clustering wedges yield a result of $(\Delta\chi^2)_{\rm min} \equiv \min(\chi^2_{\rm ref} - \chi^2) = 22.2$, meaning a 4.7σ detection of the anisotropic baryonic acoustic feature, and we obtain a similar result after applying reconstruction. This result appears to be consistent with the isotropic baryonic acoustic feature detection of CMASS-DR9 as reported by Anderson et al. (2012), who showed a 5σ detection that did not improve with reconstruction.

As seen in Fig. 5, in the pre-reconstruction case the CMASS sample appears to be on the fortunate side of the mock distribution of the detection of the anisotropic baryonic acoustic feature, where 68 per cent of the mocks lie between 2.8 and 4.6σ (i.e. a median and rms of $3.7\sigma \pm 0.9\sigma$). In the post-reconstruction case, we see a clear shift of the mocks between 3.6 and 5.4σ ($4.5\sigma \pm 0.9\sigma$). This improvement is also quantified by the fact that 23 per cent (138/600) of the pre-reconstruction mocks yield a detection of a peak with a significance lower than 3σ, whereas post-reconstruction only 4.6 per cent do (28/600; Fig. 6). Although we see clear improvement in the average mock realization, the significance of the detection of the anisotropic baryonic acoustic feature in the data does not improve after applying reconstruction. We find this non-improvement, however, consistent with 89/600 (15 per cent) of the mock realizations (Fig. 6). This demonstrates the potential of the reconstruction technique to improve constraints of $\alpha_{||}$ and $\alpha_\perp$, though we do not expect tighter constraints from the DR9 data due to the lack of enhancement in the detection of the anisotropic baryonic acoustic feature.

For later reference, we define a subsample of 462 realizations with a $\geq 3\sigma$ detection as the '$\geq 3\sigma$ subsample', and its complement the '$<3\sigma$' subsample. For a consistent comparison between the various methods these subsamples are defined when using the pre-reconstruction wedges RPT-based method. In the context of the DR9-CMASS volume, we find this separation useful for interpretation of the $\alpha_{||}$ and $\alpha_\perp$ results. For a visual of the subsamples in terms of $\Delta\chi^2$, see Fig. 6.

In the following section, we analyse how well we expect to measure $\alpha_{||}$ and $\alpha_\perp$ both pre- and post-reconstruction.

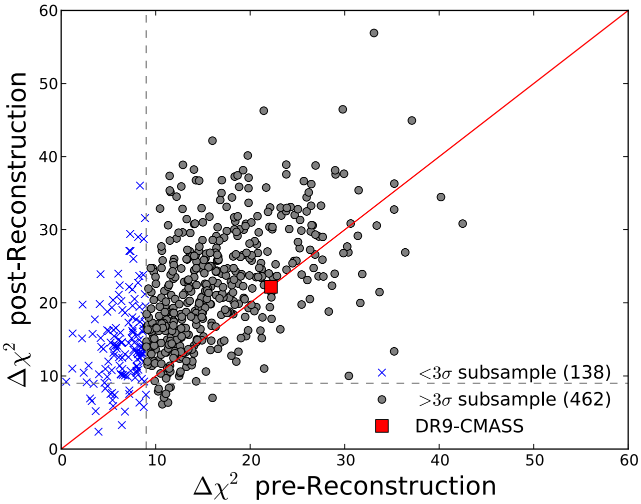

Figure 6. Here, we show a quantification of the detection of the anisotropic baryonic acoustic feature for all 600 mocks, and the data both pre- and post-reconstruction. We define the $\geq 3\sigma$ subsample as 462 realizations for which the anisotropic baryonic acoustic feature is detected with at least $\Delta\chi^2 = 9$ in the pre-reconstruction case (grey circles). The complementary are defined as the $<3\sigma$ subsample (blue crosses).

6.2 Measuring H, D_A: testing methodology on mocks

To test the various assumptions made throughout the analysis we first apply the pipeline to mock catalogues. To differentiate between systematic effects and peculiarities due to mocks with low baryonic acoustic feature signal, in Appendix C we investigate high S/N mocks to answer the following questions (answers based on results in Table C1).

Does the method outlined in Section 5.3 affect the AP test?
The RPT-based result entries show that the marginalization over the shape information yields small biases (<0.5 per cent) in the geometric information measured.

Is one ξ template preferred over the other?
We find that although the RPT-based and dewiggled templates yield similar constraints and strong mode correlations, the dewiggled one yields a ~1 per cent bias in measuring $\alpha_{||}$ (Appendix C1). The dewiggled template does not have a mode coupling term, which might explain tendencies to yield more biased mock results than the RPT-based template. In Section 6.3.3, we report results with varied $A_{\rm MC}$, but defer a more intensive investigation of possible effects for future studies [e.g. the Taruya, Nishimichi & Saito (2010) model].

Is one ξ combination preferred over the other?
We find that $\xi_{\Delta\mu}$ and ξ_ℓ contain similar constraining power (Appendix C2).

Are the resulting distributions of the $\alpha_{||}$ and $\alpha_\perp$ Gaussian?
We find that results of high S/N mocks yield close to Gaussian (or symmetric) posterior distributions but DR9-volume mocks do not. This result is probably due to the fact that the DR9 mock volumes contain a large fraction of mocks with low S/N anisotropic baryonic acoustic feature.

Does reconstruction improve/bias the above?
We find that the reconstructed RPT-based template yields a good description of the PTHalo mocks and, on average, improves constraints of $cz/H/r_s$ and D_A/r_s by ~30 per cent (Appendix C3).

These tests show that the methods applied work well on high S/N mocks. Analysing 600 PTHalo DR9 volumes, we find that a non-negligible amount of realizations yield low anisotropic baryonic acoustic feature signals.

Fig. 7 shows correlations between $\alpha_{||}$ and $\alpha_\perp$ modes (top) and their uncertainties (bottom). Numerical summaries of these results can be found in Table 2. All results correspond to using the $\xi_{\Delta\mu}$ RPT-based template (see rows under the 'Full sample, no priors' label).

As explained in Appendix C (and apparent in Fig. C1), these distributions of $\Delta\alpha_{||}/\alpha_{||}$ and $\Delta\alpha_\perp/\alpha_\perp$ are not Gaussian. A visual inspection of various individual mocks reveals some cases with weak line of sight and/or transverse baryonic acoustic features. This is quantified in Section 6.1, where we find that ~23 per cent of the realizations have an anisotropic baryonic feature with a significance of less than 3σ. For this reason, we separate the results to the $\geq 3\sigma$ subsample (grey points) and its complementary $<3\sigma$ subsample (blue points) (see rows under the label '$\geq 3\sigma$ subsample, no priors' in Table 2). Note that in both the pre- and post-reconstruction cases, both the subsamples correspond to the same as that in the pre-reconstruction case (for a visual see Fig. 6). This separation points to interesting trends in the distributions of the $\alpha_{||}$ and $\alpha_\perp$ modes and uncertainties.

Most of the outliers that measure $\alpha_{||}$ and $\alpha_\perp$ modes at >10 per cent from the true values tend to be from the $<3\sigma$ subsample in both pre- and post-reconstruction. The plot clearly shows that reconstruction substantially improves both mode and uncertainty scatters and constraints.

The uncertainty–uncertainty plots also show that most of the extremely large uncertainties are in the $<3\sigma$ subsample. Although post-reconstruction removes the trend differences in the uncertainties, we clearly see that the tightest constraints are on the $\geq 3\sigma$ subsample.

To clarify the interpretation of these results, we investigate application of a weak $|\epsilon| < 0.15$ prior on the MCMC propositions. In the mode–mode plots this limit is shown by the dashed lines. In Section 5.3.2, we discuss the observational motivation for this prior. Figs 8 and 9 show the $\alpha_{||}$ mode and uncertainty distributions, respectively, both with and without the $|\epsilon| < 0.15$ prior. Without this prior, we find a systematic 'pile-up' on the flat prior limit of $\alpha_{||} = 0.5$, which is dominated by the $<3\sigma$ subsample (blue bars). We verify that these mocks have line-of-sight baryonic acoustic features that are either washed out, or contain a $\xi_{||}$ with a spurious strong clustering measurement at $110 < s < 200\,h^{-1}$Mpc. For some of the 'double-mode' realizations (meaning with both at line-of-sight baryonic acoustic feature signal and a spurious strong feature) the ϵ prior strengthens the true mode. For realizations with strong spurious features, the ϵ prior causes them to move from $\alpha_{||} = 0.5$ closer to the $\epsilon = -0.15$ boundary.

Figs 8 and 9 and Table 2 also demonstrate that, although our method performs much better overall when applied to the $>3\sigma$ subsample than to the $<3\sigma$ subsample, there are a few pre-reconstruction realizations in which the median $\alpha_{||}$ mode and uncertainty results improve with the $|\epsilon| < 0.15$ prior. We emphasize that the post-reconstruction median $\alpha_{||}$ mode and uncertainty results do not improve with the $|\epsilon| < 0.15$ prior, and neither those of $\alpha_\perp$ pre- or post-reconstruction, although the scatter in all the statistics do. This indicates that, although the 3σ threshold is useful for separating between well-constrained realization to poor ones, it is not instructive against cases which have strong spurious line-of-sight clustering measurements.

All the above trends appear in both templates examined (RPT-based, dewiggled), and in both clustering wedges and multipoles.

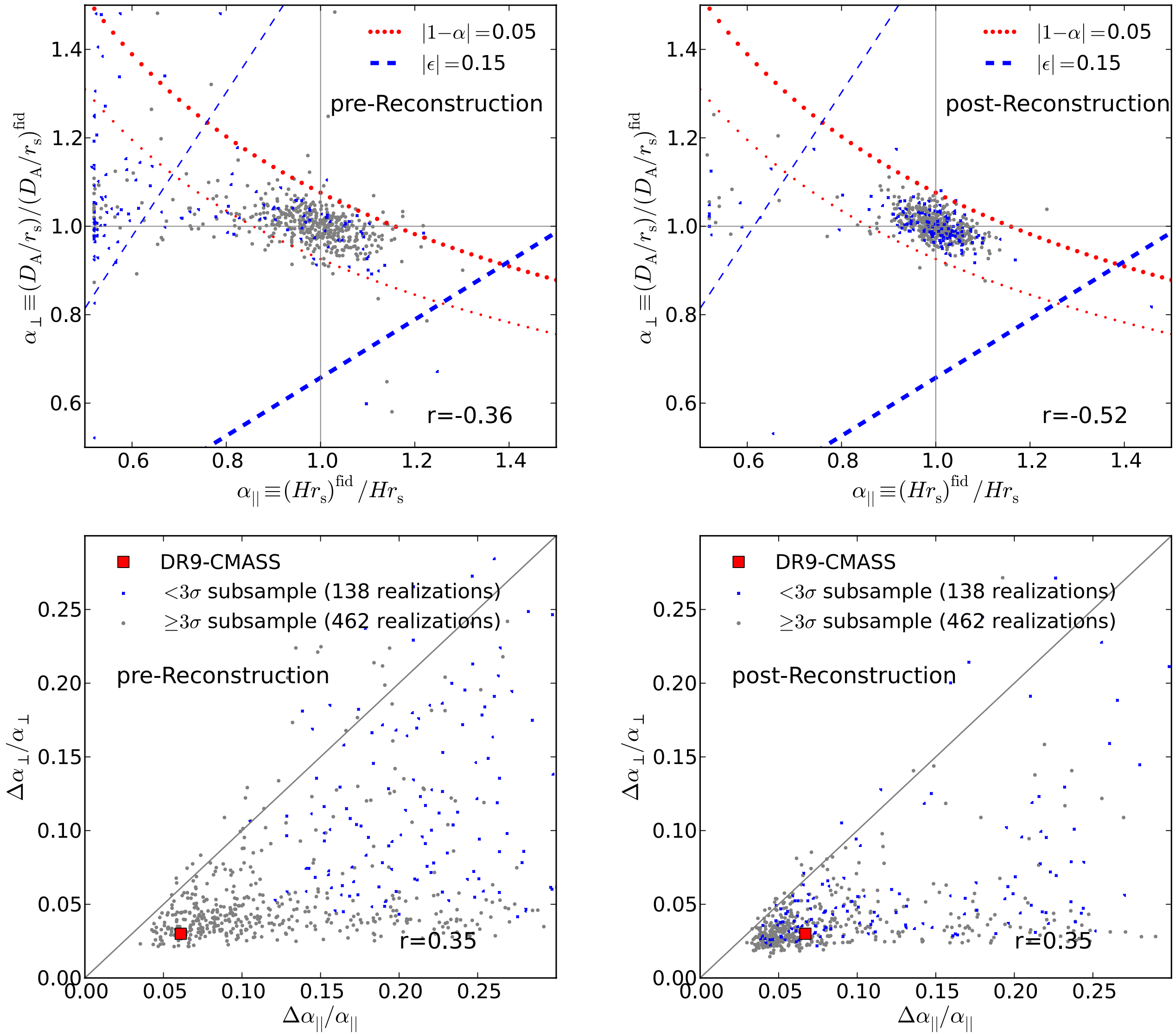

Figure 7. Pre- (left) and post-reconstruction (right) distributions of $\alpha_{||} = (Hr_\mathrm{s})^\mathrm{fid}/(Hr_\mathrm{s})$ and $\alpha_\perp = (D_\mathrm{A}/r_\mathrm{s})/(D_\mathrm{A}/r_\mathrm{s})^\mathrm{fid}$ modes and their uncertainties of the mock PTHalos using the RPT-based $\xi_{||}$, $\xi_\perp$. The top panels show the scatter of mode measurements; the bottom presents the scatter of uncertainties. Each panel presents the results of all 600 mock realizations, where the grey dots are the $\geq 3\sigma$ subsample (462 realizations) and blue for the complementary $<3\sigma$ subsample. The cross-correlation coefficient for the $\geq 3\sigma$ subsample in each panel is indicated by r. Numerical results are summarized in Table 2. In the top panels we emphasize the constant α and ϵ lines, as indicated (where the thicker line of each indicates the larger value). In the bottom panels, we mark the DR9-CMASS uncertainty measurement (red filled squares). Modes and uncertainties shown are without applying a prior on ϵ.

In Table 2, we summarize the mock results of $\alpha_{||}$ and $\alpha_\perp$ modes and uncertainties and their scatter obtained with all the methods of analysis used. Most entries are for the RPT-based clustering wedges pre- and post-reconstruction. For completeness, the first and last entries include the dewiggled templates as well as including results of multipoles in both templates. The sample examined is indicated (e.g. full sample or the $\geq 3\sigma$ subsample) as well as if a prior on ϵ is used. For example, we investigate various $|\epsilon|$ priors, or restricting to realizations with $\alpha_{||}$ and $\alpha_\perp$ modes within 14 per cent from the true values, or both.

Regarding the post-reconstruction RPT-based $\xi_{||,\perp}$ we notice that $\alpha_{||}$ has in all cases a median mode bias of ≤ 0.3 per cent, and $\alpha_\perp \leq 0.1$ per cent. Pre-reconstruction mode results, on the other hand, improve substantially when applying the various priors and cuts ($\geq 3\sigma$ subsample, $|\epsilon| < 0.15$, mode limitation). These results show the effects of mocks with low anisotropic baryonic acoustic feature signal. For example, when limiting the sample to the most constrained 2/3 of the realizations (meaning 394/600), the bias on $\alpha_{||}$ improves from 3 to 0.4 per cent and of $\alpha_\perp$ from 0.6 to ≤ 0.1 per cent.

The $\alpha_{||}$ and $\alpha_\perp$ uncertainties improve in different manners when applying the various priors and cuts. The most noticeable trend, which is common for both parameter results, is the reduction of the scatter on the uncertainty when applying the $|\epsilon| < 0.15$ prior.

For ill-constrained DR9 volumes the median uncertainties vary with choice of ϵ. On the other hand, for well-constrained realizations, such as CMASS-DR9, results do not depend on the ϵ prior (see Section 6.3).

We also find that the dewiggled pre-reconstruction template yields similar $\alpha_{||}$ and $\alpha_\perp$ constraints as the RPT-based ones, although the dewiggled pre-reconstruction template shows a systematic bias of ~1 per cent on $\alpha_\perp$. This effect is not apparent in the

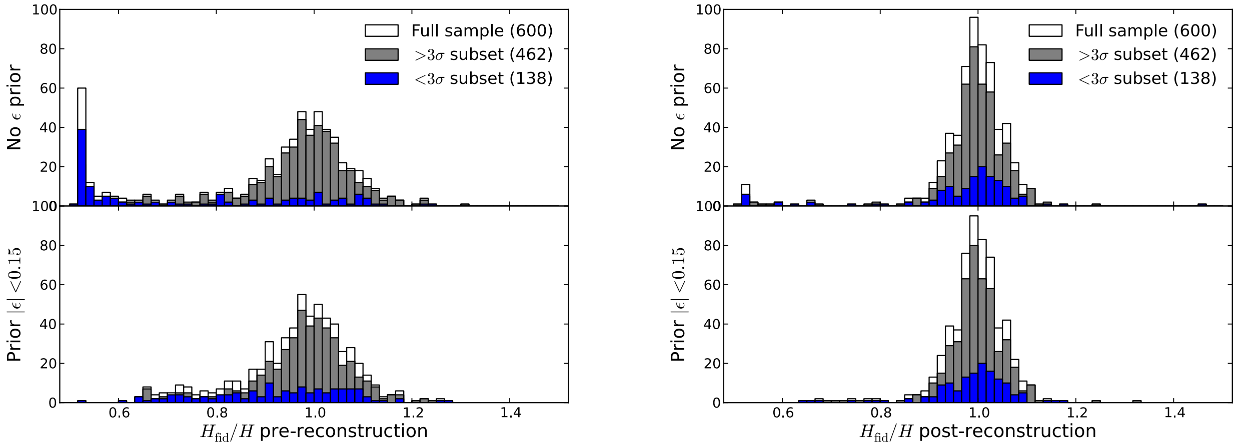

Figure 8. Pre- (left) and post-reconstruction (right) distributions of $\alpha_{||} = (Hr_s)^{\rm fid}/(Hr_s)$ modes of the mock PTHalos using the RPT-based $\xi_{||}$, $\xi_{\perp}$. The top panels show histograms of the results without using a prior on ϵ, where the bottom uses a weak prior of $|\epsilon| < 0.15$. In each we present the histogram of the full sample (white bars), the $>3\sigma$ subsample (grey) and the $<3\sigma$ subsample (blue).

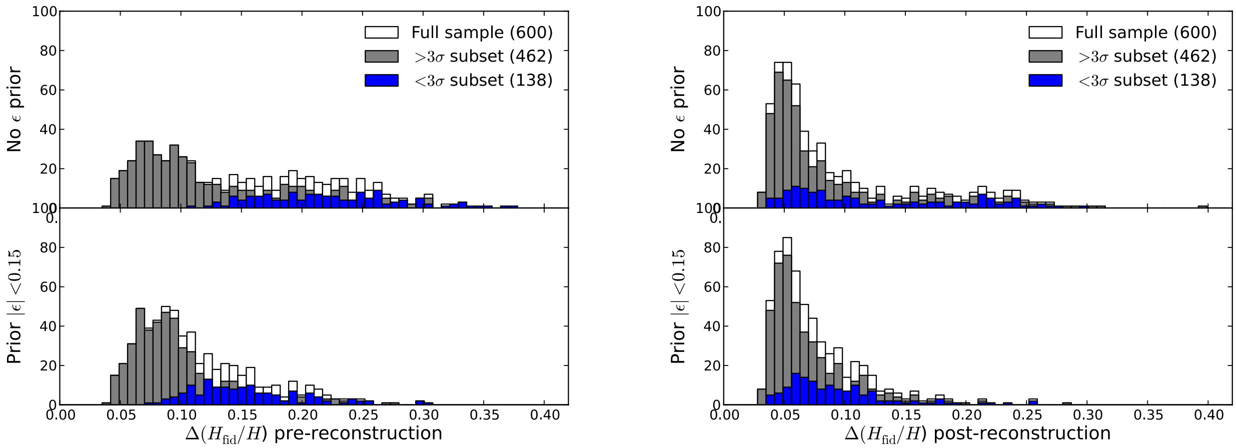

Figure 9. Pre- (left) and post-reconstruction (right) distributions of $\alpha_{||} = (Hr_s)^{\rm fid}/(Hr_s)$ uncertainties of the mock PTHalos using the RPT-based $\xi_{||}$, $\xi_{\perp}$. The top panels show histograms of the results without using a prior on ϵ, where the bottom uses a weak prior of $|\epsilon| < 0.15$. In each we present the histogram of the full sample (white bars), the $>3\sigma$ subsample (grey) and the $<3\sigma$ subsample (blue).

high S/N mocks (Appendix C2), which yield a median 1.4 per cent bias on $\alpha_{||}$, which is not apparent here. The post-reconstruction dewiggled wedges results are in line with the RPT-based.

Perhaps the most notable feature in Table 2 is that the scatter in the $\alpha_{||}$ modes is different from the median of the uncertainties. Focusing on the most constrained subsample (the bottom entry), we see that the scatter in the $\alpha_{||}$ modes is smaller than the median of the uncertainties in all cases. In Section 6.4 and Appendix C, we show that this should improve with higher S/N samples. For $\alpha_{\perp}$ we see that the scatter of the modes and median of the uncertainties are fairly similar.

The *fiducial* cosmology of the analyses is the *true* cosmology of the mocks. We defer testing possible effects of using an incorrect fiducial cosmology (for preliminary tests on mocks see Kazin et al. 2012).

To summarize, we find that a significant minority of DR9-CMASS pre-reconstruction realizations yield unreliable results. However, the majority $>3\sigma$ subsample yields a low bias result ($<$0.5 per cent). Moreover, the results show that the post-reconstruction wedges results yield low bias ($<$0.3 per cent) with both RPT-based and dewiggled. We also find that for a DR9 volume we expect non-Gaussian likelihood profiles of $cz/H/r_s$ and D_A/r_s in both pre- and post-reconstruction. We next turn to apply the same method used here on the data both pre- and post-reconstruction.

6.3 DR9-CMASS $\boldsymbol{H}$, $\boldsymbol{D_A}$ results

In this section, we present our measurements of $cz/H/r_s$ and D_A/r_s in the DR9 CMASS data set.

Our main pre- and post-reconstruction results are summarized in Figs 2 and 10. Post-reconstruction we measure $cz/H/r_s = 12.28 \pm 0.82$ (6.7 percent accuracy; uncertainties are quoted at 68 per cent CL) and $D_A/r_s = 9.05 \pm 0.27$ (3.0 percent accuracy). The correlation coefficient between $cz/H/r_s$ and D_A/r_s is measured at -0.5, similar to that predicted by Seo & Eisenstein (2007). The best-fitting model shows an excellent fit at $\chi^2/\text{d.o.f.} = 0.82$ with d.o.f. = 66 degrees of freedom. Compared to the mocks realizations, this result is lower than 398/600 of the mocks. With the pre-reconstruction $\xi_{\Delta\mu}$ we obtain $\chi^2/\text{d.o.f.} = 0.64$ (lower than 578/600 realizations). We find that the mean reduced χ^2 both pre- and post-reconstruction are at $\sim$0.9 with a scatter of $\sim$0.14. This means that the pre-reconstruction fit is on the fortunate side of sample variance and the post-reconstruction fit is as expected.

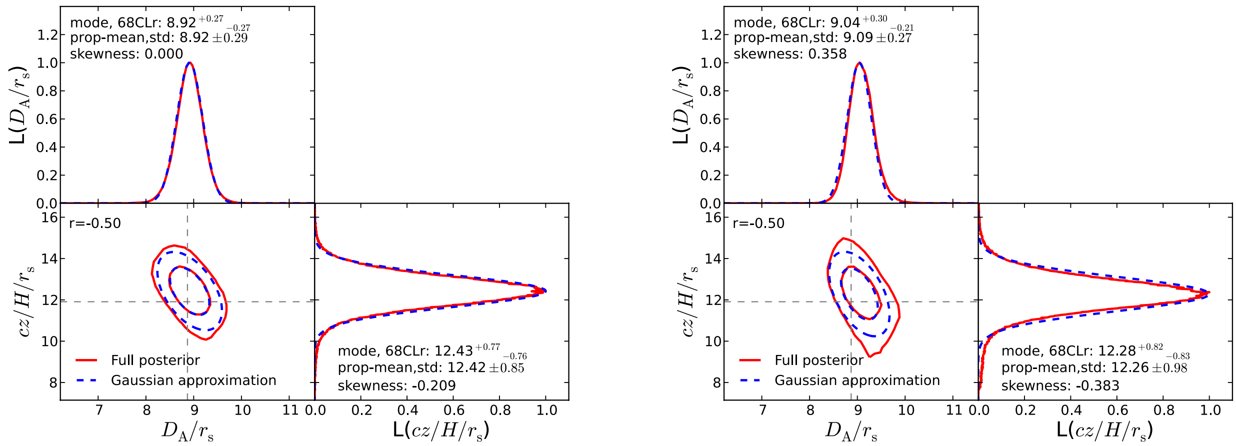

Figure 10. CMASS results pre- (left) and post-reconstruction (right). The marginalized results of $cz/H/r_s$ (right-hand panels) and D_A/r_s (top panels), and the joint constraints (bottom panels). The solid red lines are the posterior and the dashed blue lines are a Gaussian approximation, as described in the text. The panels indicate the modes, 68 per cent CL region boundaries (68CLr), proposition mean, proposition standard deviation, skewness and cross-correlation coefficient (r). The contours indicate the 68.27, 95.45 per cent CL regions. For plotting purposes, the post-reconstruction likelihoods assume a prior $|\epsilon| < 0.15$. The grey dashed lines indicate the fiducial cosmology.

This is similar to our conclusions regarding the significance of the detection of the baryonic acoustic feature seen in Section 6.1.

Fig. 10 compares the posterior results (solid red lines) with a Gaussian approximation (dashed blue lines), based on the same quoted modes, uncertainties and cross-correlation coefficients. In both the pre- and post-reconstruction cases, we see that the Gaussian approximation describes the 68.27 per cent CL region fairly well, but clearly underestimates the 95.45 per cent CL region. We also note that the full posterior 99.73 per cent CL regions obtained both pre- and post-reconstruction are not well defined. These indicate the limited S/N in these measurements. We expect the agreement to improve with larger samples. For plotting purposes, the post-reconstruction result is presented with the weak prior $|\epsilon| < 0.15$. In Table 3, we present mode and uncertainty results with and without this prior, and conclude that it does not affect these, but rather limits the 99.73 per cent CL region.

In the top plot of Fig. 11, we show a direct comparison of the likelihood profiles pre- and post-reconstruction of the RPT-based clustering wedges. Both results appear to be similar, well within the 68 per cent CL region, although in the post-reconstruction case $cz/H/r_s$ is not as tightly constrained.

For an average $>3\sigma$ detection DR9-volume mock realization we find that a mode cross-correlation of $r_{\alpha_{||}},r_{\alpha_\perp} \sim 0.4$–$0.5$ (or $\sim$0.6 when examining the high S/N mocks; Appendix C3) should be

Table 3. CMASS DR9 $\langle z\rangle = 0.57$ results.

ξ	$\alpha_{\|\|}$	$cz/H/r_s$	$\alpha_\perp$	D_A/r_s	$r_{\alpha_{\|\|},\alpha_\perp}$	H	D_A
No prior on ϵ:						(km s^{-1} Mpc^{-1})	(Mpc)
RPT-based $\xi_{\|\|,\perp}$ pre-rec	1.042	12.41 ± 0.75 (6.1 per cent)	1.006	8.92 ± 0.27 (3.0 per cent)	−0.50	89.9 ± 5.6	1367 ± 45
RPT-based $\xi_{0,2}$ pre-rec	1.072	12.77 ± 1.15 (9.0 per cent)	0.989	8.77 ± 0.36 (4.1 per cent)	−0.72	87.4 ± 7.9	1344 ± 57
Dewig $\xi_{\|\|,\perp}$ pre-rec	1.055	12.57 ± 0.73 (5.8 per cent)	1.014	8.99 ± 0.28 (3.1 per cent)	−0.57	88.8 ± 5.3	1378 ± 46
Dewig $\xi_{0,2}$ pre-rec	1.070	12.74 ± 1.06 (8.3 per cent)	1.008	8.94 ± 0.33 (3.7 per cent)	−0.72	87.5 ± 7.4	1370 ± 53
RPT-based $\xi_{\|\|,\perp}$ post-rec	1.031	12.28 ± 0.83 (6.8 per cent)	1.020	9.05 ± 0.25 (2.8 per cent)	−0.51	90.8 ± 6.2	1386 ± 42
RPT-based $\xi_{0,2}$ post-rec	0.974	11.60 ± 1.44 (12.4 per cent)	1.055	9.36 ± 0.34 (3.6 per cent)	−0.67	96.2 ± 12.0	1434 ± 55
Dewig $\xi_{\|\|,\perp}$ post-rec	1.026	12.22 ± 0.96 (7.8 per cent)	1.020	9.05 ± 0.24 (2.7 per cent)	−0.54	91.3 ± 7.3	1386 ± 41
Dewig $\xi_{0,2}$ post-rec	0.974	11.60 ± 0.79 (6.8 per cent)	1.046	9.28 ± 0.27 (3.0 per cent)	−0.62	96.2 ± 6.7	1422 ± 45
Prior $\|\epsilon\| \leq 15$ per cent:							
RPT-based $\xi_{\|\|,\perp}$ pre-rec	1.042	12.41 ± 0.75 (6.1 per cent)	1.006	8.92 ± 0.27 (3.0 per cent)	−0.50	89.9 ± 5.6	1367 ± 45
RPT-based $\xi_{0,2}$ pre-rec	1.072	12.77 ± 1.15 (9.0 per cent)	0.989	8.77 ± 0.36 (4.1 per cent)	−0.75	87.4 ± 7.9	1344 ± 57
Dewig $\xi_{\|\|,\perp}$ pre-rec	1.055	12.57 ± 0.72 (5.8 per cent)	1.014	8.99 ± 0.27 (3.0 per cent)	−0.53	88.8 ± 5.2	1378 ± 45
Dewig $\xi_{0,2}$ pre-rec	1.070	12.74 ± 1.06 (8.3 per cent)	1.008	8.94 ± 0.33 (3.7 per cent)	−0.72	87.5 ± 7.4	1370 ± 53
RPT-based $\xi_{\|\|,\perp}$ post-rec	1.031	12.28 ± 0.82 (6.7 per cent)	1.020	9.05 ± 0.27 (3.0 per cent)	−0.50	90.8 ± 6.2	1386 ± 45
RPT-based $\xi_{0,2}$ post-rec	0.974	11.60 ± 0.87 (7.5 per cent)	1.052	9.33 ± 0.36 (3.8 per cent)	−0.78	96.2 ± 7.3	1430 ± 57
Dewig $\xi_{\|\|,\perp}$ post-rec	1.026	12.22 ± 0.91 (7.4 per cent)	1.020	9.05 ± 0.27 (3.0 per cent)	−0.53	91.3 ± 6.9	1386 ± 45
Dewig $\xi_{0,2}$ post-rec	0.974	11.60 ± 0.73 (6.3 per cent)	1.046	9.28 ± 0.33 (3.6 per cent)	−0.63	96.2 ± 6.2	1422 ± 54

Notes. 1: We define $\alpha_{||} \equiv \alpha_{||}$ and $\alpha_\perp \equiv \alpha_\perp$. 2: Uncertainties (±) quoted correspond to half of the 68 per cent marginalized CL region, and their relative percentage in parentheses. 3: All values are unitless, unless otherwise indicated. 4: Fiducial values used at $\langle z\rangle = 0.57$: $(cz/H/r_s)^f = 11.93$, $(D_A/r_s)^f = 8.88$, based on *WMAP*5 cosmology (Komatsu et al. 2009). 5: The $H(0.57)$, $D_A(0.57)$ columns assume *WMAP*5 result: $r_s(z_d) = 153.3 \pm 2.0$ Mpc (table 3 in Komatsu et al. 2009). 6: $r_{\alpha_{||},\alpha_\perp}$ is the cross-correlation coefficient for $cz/H/r_s$ and D_A/r_s.

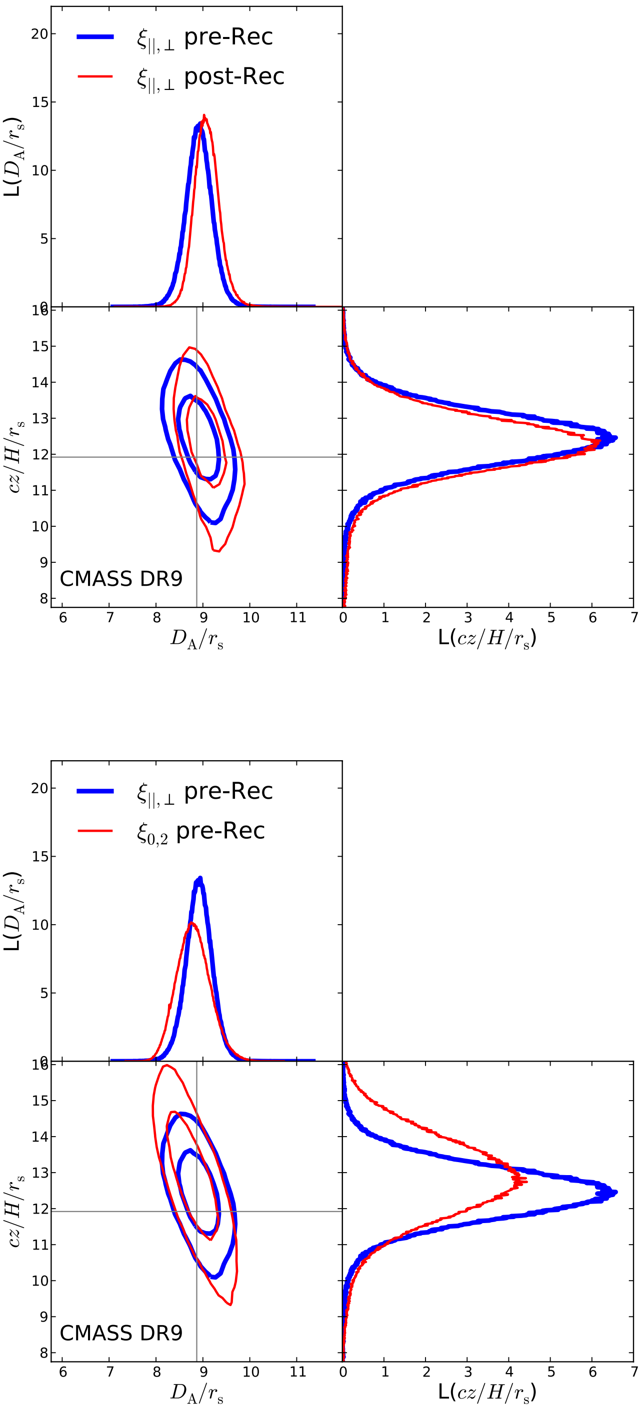

Figure 11. Comparison of the CMASS $cz/H/r_s$ and D_A/r_s results obtained with the pre-reconstruction wedges with alternative methods. The top plot shows a comparison with the post-reconstruction $\xi_{||,\perp}$ result. The bottom plot shows a comparison with the pre-reconstruction clustering multipoles ξ_0, ξ_2. All methods use the RPT-based template. The contour plots show the 68, 95 per cent CL regions. The solid lines are the fiducial cosmology.

expected, where $r_{\alpha_{||}}$ is the cross-correlation between the $cz/H/r_s$ modes obtained when using one method (here pre-reconstruction) and when using a second (here post-reconstruction), and similar for $r_{\alpha_\perp}$, when discussing D_A/r_s results. Also, although one does expect tighter constraints when applying reconstruction, the DR9 mocks indicate a 19 per cent (116/600) possibility of not improving $cz/H/r_s$. Using mocks with expected S/N of the final BOSS footprint (described in Section 6.4), this probability is reduced to ~1.5 per cent.

The CMASS $cz/H/r_s$, D_A/r_s results are summarized in Table 3 along with various related parameters.

6.3.1 *Comparing results of various ξ methods*

The results quoted in the previous section are obtained when using the $\Delta\mu = 0.5$ clustering wedges with the RPT-based template. Table 3 contains the results obtained for eight different combinations of statistics.

When applying the dewiggled template we obtain similar results to those obtained with RPT-based one. According to our mocks we expect $r_{\alpha_{||}}$,$r_{\alpha_\perp} \sim 0.85$–$0.92$ amongst the templates both pre- and post-reconstruction.

We apply the same test on the [ξ_0,ξ_2] multipoles. The bottom plot of Fig. 11 demonstrates that the pre-reconstruction joint marginalized contour of $cz/H/r_s$ and D_A/r_s obtained with ξ_ℓ agrees very well with that obtained with the clustering wedges, although the former is a bit more elongated. According to our DR9 mock catalogues, we expect that pre-reconstruction mode cross-correlations between clustering wedges results to multipoles of $r_{\alpha_{||}} \sim 0.7$, $r_{\alpha_\perp} \sim 0.7$ and uncertainty cross-correlation to be $r_{\Delta\alpha_{||}/\alpha_{||}} \sim 0.7$, $r_{\Delta\alpha_\perp/\alpha_\perp} \sim 0.3$. The difference between the uncertainties of $cz/H/r_s$ obtained by the data $\xi_{\Delta\mu}$ to those obtained with the data ξ_ℓ is 0.4, which is 3.2 per cent relative to the measurement (see Table 3). This result is consistent with the scatter obtained with the mocks (also 3.2 per cent). The difference between the data D_A/r_s uncertainties obtained with ξ_ℓ and $\xi_{\Delta\mu}$ is 1 per cent of the measurement, which within the expected 2.6 per cent scatter in the mocks. When examining high S/N costacked mocks the cross-correlations improve. This indicates that, although the clustering wedges and the multipoles should yield similar modes with the same constraining power, volume limitations and perhaps unknown errors in angular masking, might cause differences in the results.

Fig. 12 displays $cz/H/r_s$, D_A/r_s likelihood profiles of all eight different methods analysed here. The plot shows that all methods yield consistent results. The $\xi_{0,\,2}$ pre-rec (both RPT-based and dewiggled) $cz/H/r_s$ profiles appear to be wider than the rest, where the $\xi_{0,\,2}$ post-rec (both RPT-based and dewiggled) resulting modes appear to be the furthest from the rest. The post-reconstruction $cz/H/r_s$ mode difference is 0.68 (5.5 per cent of the measurement), in agreement with the expected 6.6 per cent scatter seen in the mocks. The post-reconstruction D_A/r_s mode difference is 3.1 per cent of the measurement (see Table 3), slightly higher than the expected 1.9 per cent. As argued above, these differences are as expected due to effects of sample variance, as seen in the results of the mocks (for a visual of the scatter in the higher S/N mock results see bottom plot in Fig. 14). We investigate various methods of shape parameters, and find similar results.

6.3.2 *Robustness of results to the range of fitted scales*

As discussed in Section 5.3, these measurements focus on the information of the anisotropic baryonic acoustic feature and not from the full shape. As such, we do not expect dependency of our results on the range of scales used in the analysis.

The results quoted in the previous sections are obtained when analysing data in the region of separations between

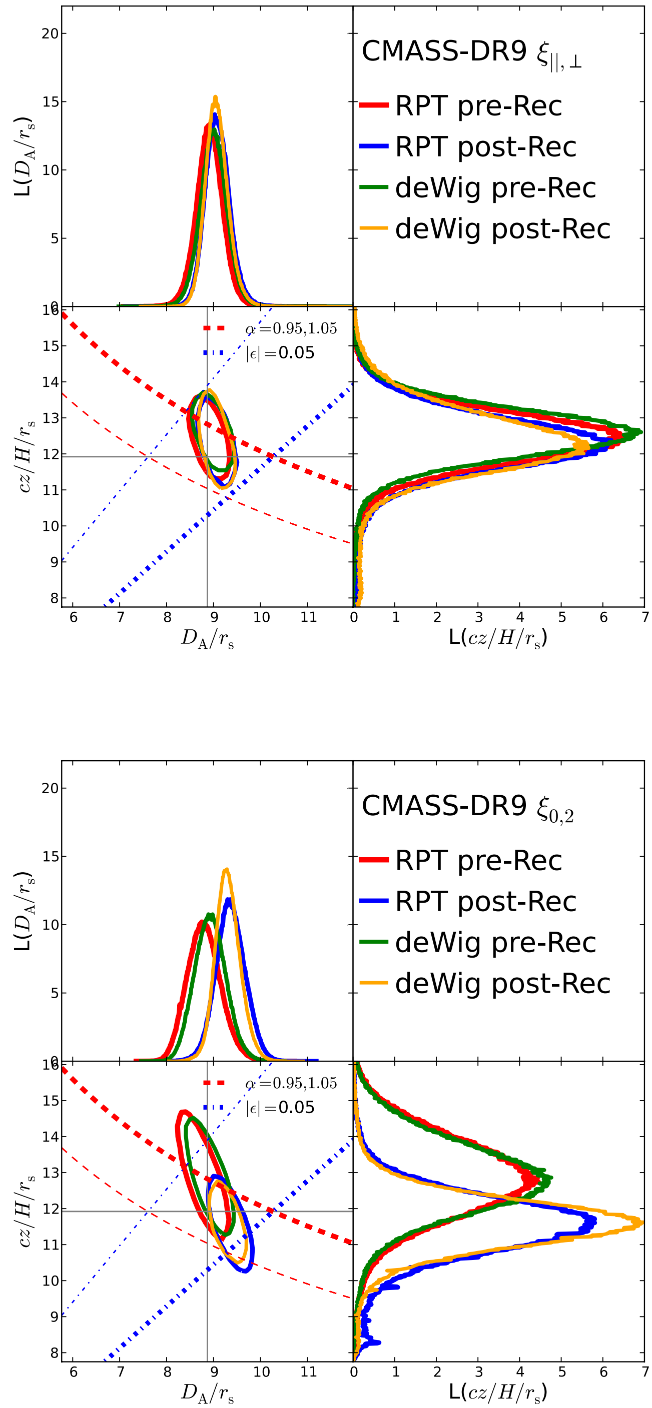

Figure 12. Comparison of the CMASS-DR9 $cz/H/r_s$ and D_A/r_s marginalized profiles obtained with all the methods tested here. The top panel shows results when using the $\xi_{\Delta\mu}$ and the bottom panel when using $\xi_{0,2}$. The contour plots show the 68 per cent CL regions. The solid lines are the fiducial cosmology. To guide the eye we plot the regions of constant α and ϵ, as indicated in the legend (where the thicker line of each indicates the larger value).

$[s_{\rm min}, s_{\rm max}] = [50, 200]$. We compare the results obtained for various choices of $s_{\rm min}$, $s_{\rm max}$. Fig. 13 shows the comparison of the results.

We find that, for the most part, the range of analysis does not affect our main results: mode values, uncertainties, cross-correlation coefficient or skewness. Regions of exception involve

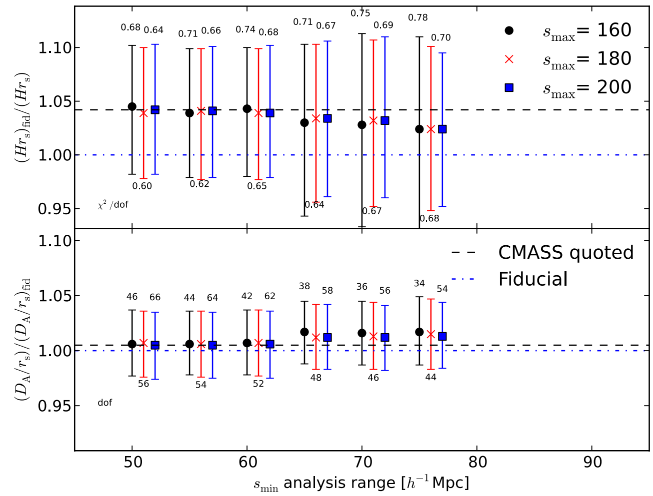

Figure 13. This plot shows that the CMASS RPT-based $\xi_{||,\perp}$ pre-reconstruction results are insensitive to the range of analysis used when $s_{\rm min} < 65$. The x-axes are the minimum separation used $s_{\rm min}$, where we compare results of $s_{\rm min} = 50, 55, 60, 65, 70, 75$ h^{-1}Mpc with maximum separations of $s_{\rm max} = 160$ (black circles), 180 (red crosses) and 200 h^{-1}Mpc (blue squares). The number of degrees of freedom (d.o.f.) and χ^2/d.o.f. are quoted. All uncertainties indicate the 68 per cent CL regions. The blue dot–dashed lines are the fiducial input values used to convert z into comoving distances, and the black dashed lines are the chosen result quoted in Table 3.

those with $s_{\rm min} \geq 65$ h^{-1}Mpc, in which the $cz/H/r_s$ uncertainties increase from ∼6 to 7 per cent and even higher, when limiting to $s_{\rm max}$=160 h^{-1}Mpc. This result could be explained by the fact that in this latter test the full dip of the baryonic acoustic feature is not used, and shape parameter values that cause spurious dips are accepted, whereas for lower values of $s_{\rm min}$ they are not. We conclude that a more reliable result would include data points along the full shape, even though that information is marginalized over through the linear bias and $A(s)$ terms.

We do not consider analyses with $s_{\rm min} < 50$ h^{-1}Mpc, because the templates used do not describe well the velocity-dispersion damping in the PTHalo mock-mean signal, and hence models would too heavily depend on the $A(s)$ terms.

In all ranges investigated the χ^2/d.o.f. is between 0.6 and 0.8, with the $s_{\rm max} = 180$ h^{-1}Mpc yielding the best fits, although not significantly better ones.

6.3.3 Regarding the nuisance and fixed parameters

As described in Section 5.3, we use a set of 10 parameters Φ_{10}. To best understand the effects and correlations of these parameters amongst themselves and with $cz/H/r_s$, D_A/r_s we examine the results of both the data and the mock-mean signal. We perform these tests both pre- and post-reconstruction in both templates for $\xi_{\Delta\mu}$ and $\xi_{0,2}$.

Overall, we do not see particular strong correlations between the $A(s)$ shape parameters with $cz/H/r_s$, D_A/r_s, where most cross-correlations are $r < 0.2$, but do illuminate a few findings of interest.

Most of the shape parameters have marginalized likelihood profiles that are fairly symmetric (low skewness). We find that amplitude parameters $a_{0||}$ and $a_{0\perp}$ are uncorrelated with each other. All correlations of these parameters with $cz/H/r_s$ and D_A/r_s are $r < 10$ per cent. The constant parameters (a_3) are uncorrelated to $cz/H/r_s$ and D_A/r_s, as expected. The other shape terms have weak correlations with $cz/H/r_s$ and D_A/r_s, (at $r < 0.2$).

The most important finding of the shape parameters, however, regards the $a_{0\,\xi_2}$ (the amplitude of the quadrupole). In both pre- and post-reconstruction its marginalized likelihood profile is not well constrained, causing strong skewness in the joint likelihoods with other parameters. We decide to fix its value, which yields results similar to $\xi_{\Delta\mu}$, where this behaviour is not present.

We find all the above similar for the data and mock mean in the pre-reconstruction case. In the post-reconstruction case this is true as well, after we apply a prior $|\epsilon| < 0.15$. Before applying the prior, the 99.7 per cent CL region is not well defined as the MCMC chains tend to accept values at the low limit set $\alpha_{||} = 0.5$.

Finally, we address the question of the $A_{\rm MC}$ parameter in the RPT-based template (equation 18). Crocce & Scoccimarro (2008) introduced this parametrization to effectively take into account the coupling between the k-modes, which results in a 0.5 per cent shift in the peak position in ξ_0. To obtain reliable templates of the post-reconstruction $\xi_{\Delta\mu}$ and ξ_ℓ we find that a model without an $A_{\rm MC}$ term yields biased results in the mocks, by about $\sim$1 per cent in $\alpha_{||}$. When analysing the post-reconstruction CMASS $\xi_{||,\perp}$ results, we see a shift in α from 1.026 ($A_{\rm MC} = 2.44$) to 1.030 ($A_{\rm MC} = 0$), a 0.4 per cent increase. The $1+\epsilon$ value is similar at 1.003. This results in a 0.3 per cent shift in $cz/H/r_{\rm s}$ and 0.2 per cent shift in $D_{\rm A}/r_{\rm s}$, well below the uncertainties. For the post-reconstruction $\xi_{0,2}$ we find similar results.

6.4 Final CMASS forecasts

By the conclusion of BOSS (2014), the survey will cover three times the area of the data set analysed here, meaning the full CMASS sample will have a volume three times as large. By stacking the PTHalo mocks in groups of three, we can roughly forecast the $cz/H/r_{\rm s}$, $D_{\rm A}/r_{\rm s}$ results of the full CMASS galaxy sample. Using the 600 realizations, we analyse here results of 200 $\xi_{||,\perp}$ stacked mocks.

It is important to emphasize that the estimates yielded here should be considered *maximum* bounds. We argue this due to the fact that the C_{ij} used is the same DR9 volume covariance matrix as in equation (15) but divided by three. This means that we do not account for noisy cross-correlations which should be reduced with the actual full CMASS geometry, thus we expect the constraining power to be tighter when using a more reliable C_{ij}.[6] Furthermore, we note that replicating the DR9 geometry does not improve the reconstruction boundary effects.

Fig. 14 displays the $cz/H/r_{\rm s}$ and $D_{\rm A}/r_{\rm s}$ results obtained by means of the expected modes and uncertainties, comparing between post- and pre-reconstruction $\xi_{||,\perp}$ (top), and post-reconstruction $\xi_{||,\perp}$ to $\xi_{0,2}$ (bottom).

When comparing $cz/H/r_{\rm s}$, $D_{\rm A}/r_{\rm s}$ results of the $\xi_{0,2}$ to the $\xi_{||,\perp}$ we find strong correlations where mode biases are sub 0.3 per cent. Uncertainties show that no method is preferred over the other. When comparing pre- and post-reconstruction wedges, we find an $r \sim 0.52$ between the modes.

When applying reconstruction, the $cz/H/r_{\rm s}$ uncertainties are predicted to improve from 0.045 ± 0.017 to 0.030 ± 0.006, a 33 per cent improvement. For $D_{\rm A}/r_{\rm s}$ the improvement is forecast to be from 0.024 ± 0.007 to 0.017 ± 0.003, a $\sim$30 per cent improvement. The

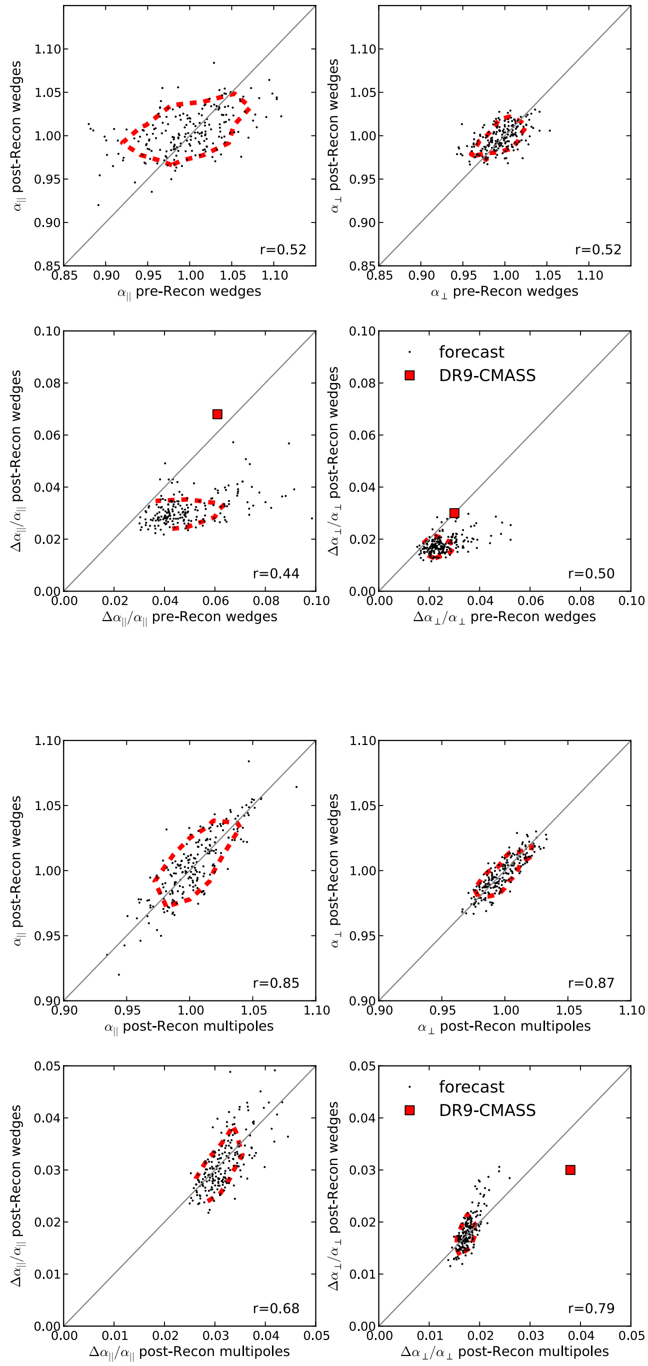

Figure 14. $\alpha_{||} \equiv \alpha_{||}$ and $\alpha_\perp \equiv \alpha_\perp$ mode and fractional uncertainty forecasts of 200 pseudo-final BOSS CMASS volumes. In all plots the *y*-axis results are for post-reconstruction wedges. In the top plot, the *x*-axis results are for pre-reconstruction wedges, at the bottom post-reconstruction multipoles. In each plot, the comparisons are between $\alpha_{||}$ modes (top-left panels), $\alpha_\perp$ modes (top right), $\Delta\alpha_{||}/\alpha_{||}$ uncertainties (bottom left), $\Delta\alpha_\perp/\alpha_\perp$ uncertainties (bottom right). The cross-correlation in each is *r*. The dashed red lines are the 68 per cent CL regions. For the comparison, the red boxes are the DR9-CMASS results.

mock result distributions yield Gaussian-like features, although application of the Kolmogorov–Smirnov (K–S) tests indicates they are not Gaussian. These trends are similar to those seen with 100 six-stacked mocks (see Appendix C).

[6] A better estimate would include a covariance matrix that would take into account the expected larger survey footprint which will reduce potential angular effects.

7 DISCUSSION

The $cz/H/r_s$ and D_A/r_s results obtained here are consistent across the various techniques investigated:

(i) $\xi_{||,\perp}$, $\xi_{0,2}$,
(ii) ξ templates: RPT-based, dewiggled and
(iii) pre- and post-reconstruction.

The likelihood profiles obtained with these eight combinations investigated are shown in Fig. 12 (as well as Fig. 11 and Table 3). Differences between the results are as expected from mock simulations.

As these posteriors are not Gaussian, we provide joint 2D marginalized likelihood profiles of $cz/H/r_s$ and D_A/r_s, as well as the CMASS-DR9 $\xi_{||,\perp}$ and C_{ij}, C^{-1}_{ij} on the SDSS-III website.[7] We conclude this study by using results obtained post-reconstruction over those yielded pre-reconstruction, because we show that mock results expect an improvement of 30 per cent in the marginalized constraints of $cz/H/r_s$ and D_A/r_s, even though this is not the case in the data. We also prefer the RPT-based template over the dewiggled due to the larger bias in the mock results when using the latter. In the data, we find the posteriors to be similar regardless of the choice of the template (see Fig. 12).

Comparison of our results to other analyses of the same data set can be found in the following studies. Anderson et al. (2013) measures $cz/H/r_s$ and D_A/r_s by applying a similar model-independent method on the $\xi_{0,2}$, using the same dewiggled templates. The main differences in analysis involve their use of a grid of α and ϵ, where the rest of the nuisance parameters are determined by the least-squares method. We perform extensive comparisons between the methods, and find the $cz/H/r_s$ and D_A/r_s similar results (see fig. 13 and sections 5.2, 6.2, 6.3 in Anderson et al. 2013). Anderson et al. (2013) continue to use results obtained in both studies to produce a 'consensus result' and calculate cosmological implications.

Model-dependent analyses are performed on the full shape of $\xi_{||,\perp}$ (Sánchez et al. 2013) and $\xi_{0,2}$ (Reid et al. 2012; Chuang et al. 2013). Sánchez et al. (2013) show that results amongst these studies are compatible. Fig. 15 in Sánchez et al. (2013) shows a comparison between our pre-reconstruction model-independent result and their results from the full shape which are independent of parameter space, but assume that *f* follows GR predictions. They find an excellent agreement with our results, although tighter constraints such as the baryonic acoustic feature only method effectively accepts parameter values (e.g. Ω_M) that the full shape does not.

8 SUMMARY

In this study, we investigate the ability of the BOSS DR9-CMASS volume to constrain cosmic geometry at $z = 0.57$, through the use of the AP technique applied on the anisotropic baryonic acoustic feature. We analyse the information contained in the anisotropic baryonic acoustic feature, for the first time, using a new technique called clustering wedges $\xi_{\Delta\mu}$ and compare results to the multipoles $\xi_{0,2}$.

We find the anisotropic baryonic acoustic feature to be detected in the DR9-CMASS sample at a significance of 4.7σ compared to a featureless model (Section 6.1), consistent with that expected from the mock realizations. Although we show in the simulations that the results should improve with the application of reconstruction, the post-reconstruction detection significance is similar to that of the pre-reconstruction. A non-improvement in the significance of detection is consistent with 15 per cent (89/600) of the mock realizations. Analysis of the mock catalogues points out that a minority of the realizations have low significance of detection ($<3\sigma$) mostly due to low S/N of the line-of-sight baryonic acoustic feature. In the pre-reconstruction case, these are quantified to 23 per cent of the realizations where post-reconstruction this is reduced to less than 5 per cent (Fig. 6).

To obtain geometrical constraints that are model independent, we use information from the post-reconstruction anisotropic baryonic acoustic feature and measure $cz/H/r_s = 12.28 \pm 0.82$ (6.7 per cent accuracy) and $D_A/r_s = 9.05 \pm 0.27$ (3.0 per cent) with a correlation coefficient of -0.5 (uncertainties are quoted at 68 per cent CL). These results are consistent with those expected when analysing mock simulations. Although CMASS-DR9 results do not improve with reconstruction, mock catalogues indicate that, on average, one should expect an improvement of constraining power of $\sim$30 per cent. Throughout this study, we show that the posteriors of $cz/H/r_s$ and D_A/r_s from the DR9 volume are not expected to be Gaussian. In Section 7, we have explained how to use the results presented here, pointing out that the provided full likelihood function should be used instead of a Gaussian approximation. Anderson et al. (2013) analyse cosmological consequences of this measurement.

In our analysis of mock catalogues, we also demonstrate that the constraining power of $\xi_{0,2}$ and $\xi_{||,\perp}$ are expected to be similar. With this information we conclude that the analysis of the clustering wedges and comparison to the multipoles technique, as performed here, are vital for testing systematics when measuring $cz/H/r_s$ and D_A/r_s. Here, we use wide clustering wedges of $\Delta\mu = 0.5$, which are fairly correlated (see Fig. 3). As long as covariances can be adequately taken into account, this method could be generalized to narrower $\Delta\mu$ clustering wedges, as future surveys will yield better S/N.

ACKNOWLEDGEMENTS

It is a pleasure to thank Chris Blake for his insight. We also thank David Kirkby, Felipe Marin, Cameron McBride and Uros Seljak for useful discussions. EK is supported by the Australian Research Council Centre of Excellence for All-sky Astrophysics (CAASTRO), through project number CE110001020. AGS acknowledges support by the Trans-regional Collaborative Research Centre TR33 'The Dark Universe' of the German Research Foundation (DFG). EAK thanks Erin Sheldon for software used here. Numerical computations for the PTHalos mocks were done on the Sciama High Performance Compute (HPC) cluster which is supported by the ICG, SEPNet and the University of Portsmouth. Funding for SDSS-III has been provided by the Alfred P. Sloan Foundation, the Participating Institutions, the National Science Foundation and the US Department of Energy Office of Science. The SDSS-III website is http://www.sdss3.org/. SDSS-III is managed by the Astrophysical Research Consortium for the Participating Institutions of the SDSS-III Collaboration including the University of Arizona, the Brazilian Participation Group, Brookhaven National Laboratory, University of Cambridge, Carnegie Mellon University, University of Florida, the French Participation Group, the German Participation Group, Harvard University, the Instituto de Astrofisica de Canarias, the Michigan State/Notre Dame/JINA Participation Group, Johns Hopkins University, Lawrence Berkeley National Laboratory, Max Planck Institute for Astrophysics, Max Planck Institute for Extraterrestrial Physics, New Mexico State University, New York

[7] http://www.sdss3.org/science/boss_publications.php

University, Ohio State University, Pennsylvania State University, University of Portsmouth, Princeton University, the Spanish Participation Group, University of Tokyo, University of Utah, Vanderbilt University, University of Virginia, University of Washington and Yale University.

REFERENCES

Ahn C. P. et al., 2012, ApJS, 203, 21
Aihara H. et al., 2011, ApJS, 193, 29
Alcock C., Paczynski B., 1979, Nat, 281, 358
Anderson T. W., 2003, An Introduction to Multivariate Statistical Analysis, 3rd edn. Wiley-Interscience
Anderson L. et al., 2012, MNRAS, 427, 3435
Anderson L. et al., 2013, preprint (arXiv:e-prints)
Ballinger W. E., Peacock J. A., Heavens A. F., 1996, MNRAS, 282, 877
Bassett B., Hlozek R., 2010, in Ruiz-Lapuente P., ed., Dark Energy: Observational and Theoretical Approaches. Cambridge Univ. Press, Cambridge
Berlind A. A., Weinberg D. H., 2002, ApJ, 575, 587
Bernardeau F., Colombi S., Gaztañaga E., Scoccimarro R., 2002, Phys. Rep., 367, 1
Beutler F. et al., 2011, MNRAS, 416, 3017
Beutler F. et al., 2012, MNRAS, 423, 3430
Blake C., Glazebrook K., 2003, ApJ, 594, 665
Blake C. et al., 2011a, MNRAS, 415, 2876
Blake C. et al., 2011b, MNRAS, 415, 2892
Blake C. et al., 2011c, MNRAS, 1599
Blake C. et al., 2011d, MNRAS, 1598
Bolton A. S. et al., 2012, AJ, 144, 144
Busca N. G. et al., 2013, A&A, 552, A96
Chuang C.-H., Wang Y., 2012a, MNRAS, 426, 226
Chuang C.-H., Wang Y., 2012b, preprint (arXiv:1209.0210)
Chuang C.-H. et al., 2013, preprint (arXiv:1303.4486)
Cole S., Fisher K. B., Weinberg D. H., 1995, MNRAS, 275, 515
Cole S. et al., 2005, MNRAS, 362, 505
Cooray A., Sheth R., 2002, Phys. Rep., 372, 1
Crocce M., Scoccimarro R., 2008, Phys. Rev. D, 77, 023533
Dawson K. S. et al., 2013, AJ, 145, 10
Drinkwater M. J. et al., 2010, MNRAS, 401, 1429
Einstein A., 1916, Ann. Phys., 354, 769
Eisenstein D. J., Hu W., 1998, ApJ, 496, 605
Eisenstein D. J. et al., 2005, ApJ, 633, 560
Eisenstein D. J., Seo H.-J., White M., 2007a, ApJ, 664, 660
Eisenstein D. J., Seo H.-J., Sirko E., Spergel D. N., 2007b, ApJ, 664, 675
Eisenstein D. J. et al., 2011, AJ, 142, 72
Gaztañaga E., Cabré A., Hui L., 2009, MNRAS, 399, 1663
Gunn J. E. et al., 1998, AJ, 116, 3040
Gunn J. E. et al., 2006, AJ, 131, 2332
Guzzo L. et al., 2007, Nuovo Cimento B, 122, 1385
Hamilton A. J. S., 1998, in Hamilton D., ed., Astrophysics and Space Science Library, Vol. 231, The Evolving Universe. Kluwer, Dordrecht, p. 185
Hartlap J., Simon P., Schneider P., 2007, A&A, 464, 399
Hinshaw G. et al., 2012, preprint (arXiv:1212.5226)
Hoffman Y., Ribak E., 1991, ApJ, 380, L5
Hu W., Haiman Z., 2003, Phys. Rev. D, 68, 063004
Hu W., Sugiyama N., Silk J., 1997, Nat, 386, 37
Jones D. H. et al., 2009, MNRAS, 399, 683
Kaiser N., 1987, MNRAS, 227, 1
Kazin E. A., Blanton M. R., Scoccimarro R., McBride C. K., Berlind A. A., 2010, ApJ, 719, 1032
Kazin E. A., Sánchez A. G., Blanton M. R., 2012, MNRAS, 419, 3223
Kirkby D. et al., 2013, J. Cosmol. Astropart. Phys., preprint (arXiv:1301.3456)
Komatsu E. et al., 2009, ApJS, 180, 330
Komatsu E. et al., 2011, ApJS, 192, 18
Landy S. D., Szalay A. S., 1993, ApJ, 412, 64
Lavaux G., Wandelt B. D., 2012, ApJ, 754, 109
Linder E. V., 2008, Astropart. Phys., 29, 336
Manera M. et al., 2013, MNRAS, 428, 1036
Masters K. L. et al., 2011, MNRAS, 418, 1055
Mehta K. T., Seo H.-J., Eckel J., Eisenstein D. J., Metchnik M., Pinto P., Xu X., 2011, ApJ, 734, 94
Noh Y., White M., Padmanabhan N., 2009, Phys. Rev. D, 80, 123501
Nuza S. E. et al., 2013, MNRAS, 432, 743
Okumura T., Matsubara T., Eisenstein D. J., Kayo I., Hikage C., Szalay A. S., Schneider D. P., 2008, ApJ, 676, 889
Padmanabhan N., White M., 2008, Phys. Rev. D, 77, 123540
Padmanabhan N., White M., Cohn J. D., 2009, Phys. Rev. D, 79, 63523
Padmanabhan N., Xu X., Eisenstein D. J., Scalzo R., Cuesta A. J., Mehta K. T., Kazin E., 2012, MNRAS, 427, 2132
Park C., Vogeley M. S., Geller M. J., Huchra J. P., 1994, ApJ, 431, 569
Peacock J. A., Smith R. E., 2000, MNRAS, 318, 1144
Peebles P. J. E., Yu J. T., 1970, ApJ, 162, 815
Perlmutter S. et al., 1999, ApJ, 517, 565
Phillipps S., 1994, MNRAS, 269, 1077
Reid B. A. et al., 2012, MNRAS, 426, 2719
Riess A. G. et al., 1998, AJ, 116, 1009
Samushia L., Percival W. J., Raccanelli A., 2012, MNRAS, 420, 2102
Samushia L. et al., 2013, MNRAS, 429, 1514
Sánchez A. G., Baugh C. M., Angulo R., 2008, MNRAS, 390, 1470
Sánchez A. G. et al., 2012, MNRAS, 425, 415
Sánchez A. et al., 2013, MNRAS, 433, 1202
Scoccimarro R., Sheth R. K., Hui L., Jain B., 2001, ApJ, 546, 20
Seljak U., 2000, MNRAS, 318, 203
Seo H., Eisenstein D. J., 2007, ApJ, 665, 14
Seo H. et al., 2010, ApJ, 720, 1650
Shoji M., Jeong D., Komatsu E., 2009, ApJ, 693, 1404
Slosar A. et al., 2013, J. Cosmol. Astropart. Phys., 4, 26
Smee S. et al., 2013, AJ, 146, 32
Taruya A., Nishimichi T., Saito S., Hiramatsu T., 2009, Phys. Rev. D, 80, 123503
Taruya A., Nishimichi T., Saito S., 2010, Phys. Rev. D, 82, 063522
Taruya A., Saito S., Nishimichi T., 2011, Phys. Rev. D, 83, 103527
Wagner C., Müller V., Steinmetz M., 2008, A&A, 487, 63
Weinberg D. H., Mortonson M. J., Eisenstein D. J., Hirata C., Riess A. G., Rozo E., 2012, preprint (arXiv:1201.2434)
White M. et al., 2011, ApJ, 728, 126
Xu X., Padmanabhan N., Eisenstein D. J., Mehta K. T., Cuesta A. J., 2012, MNRAS, 427, 2146
Xu X., Cuesta A. J., Padmanabhan N., Eisenstein D. J., McBride C. K., 2013, MNRAS, 431, 2834
York D. G. et al., 2000, AJ, 120, 1579
Zaroubi S., Hoffman Y., Fisher K. B., Lahav O., 1995, ApJ, 449, 446

APPENDIX A: THE AP MAPPING IN PRACTICE

Here, we describe the geometrical correction mapping (or AP shifting) of 1D statistics as $\xi_{||,\perp}$, $\xi_{0,2}$.

As we compare a ξ template to data which are affected by geometrical distortions we must distinguish between two sets of coordinate systems, which are, ultimately, related through H and $D_{\rm A}$.

In Section 2, we have defined the geometric distortions of the components of $\boldsymbol{s}$. In the final product, though, we use its absolute value and μ related by

$$s \equiv |\boldsymbol{s}| = \sqrt{s_{||}^2 + s_{\perp}^2}, \quad \mu = \frac{s_{||}}{s}, \tag{A1}$$

where $s_{||}$ is the line-of-sight separation component.

The template, from which the model is constructed, is calculated in a 'true' or 'test' coordinate system $s_{\rm t}$, $\mu_{\rm t}$, where the data are in shifted axes based on the fiducial cosmology, hence we define its separations and angles $s_{\rm f}$, $\mu_{\rm f}$. Because we apply the model to the data, the model, which is based on the template, should be in the fiducial coordinate system, as well, hence the AP shifting of the template to $\xi^{\rm template}(s_{\rm f}, \mu_{\rm f})$.

Using equations (3)–(6) along with equations (A1) we obtain

$$s_{\rm t} = s_{\rm f} \cdot \sqrt{\alpha_{||}^2\mu_{\rm f}^2 + \alpha_{\perp}^2\left(1-\mu_{\rm f}^2\right)} \quad \text{(A2)}$$

and

$$\mu_{\rm t} = \mu_{\rm f}\frac{\alpha_{||}}{\sqrt{\alpha_{||}^2\mu_{\rm f}^2 + \alpha_{\perp}^2\left(1-\mu_{\rm f}^2\right)}}. \quad \text{(A3)}$$

After $\xi^{\rm template}(s_{\rm f}, \mu_{\rm f})$ is produced (see below for details of its construction), we calculate

$$\xi_{\Delta\mu}^{\mathcal{AP}\ \rm template}(s_{\rm f}) = \frac{1}{\Delta\mu}\int_{\mu_{\rm f\ min}}^{\mu_{\rm f\ min}+\Delta\mu} \xi^{\rm template}(s_{\rm f}, \mu_{\rm f})\,{\rm d}\mu_{\rm f} \quad \text{(A4)}$$

for the clustering wedges. For the multipoles we calculate

$$\xi_{\ell}^{\mathcal{AP}\ \rm template}(s_{\rm f}) = (2\ell+1)\int_0^1 \xi^{\rm template}(s_{\rm f}, \mu_{\rm f})\mathcal{L}_{\ell}(\mu_{\rm f})\,{\rm d}\mu_{\rm f}. \quad \text{(A5)}$$

To calculate $\xi^{\rm template}(s_{\rm f}, \mu_{\rm f})$ in practice we apply the following steps.

(i) At every point of the integration we use equations (A2)–(A3) to convert the fiducial $s_{\rm f}$, $\mu_{\rm f}$ into the template true coordinates $s_{\rm t}$, $\mu_{\rm t}$.

(ii) We interpolate stored arrays of a pre-calculated ξ_0, ξ_2 templates to the resulting $s_{\rm t}$ value. For details regarding the templates used see Section 5.2.

(iii) We calculate $\xi(s_{\rm f}, \mu_{\rm f})$ by interpolation of $\xi(s_{\rm t}(s_{\rm f}, \alpha_{||}, \alpha_{\perp}, \mu_{\rm f}), \mu_{\rm t}(\alpha_{||}, \alpha_{\perp}, \mu_{\rm f})) = \xi_0(s_{\rm t}) + \mathcal{L}_2(\mu_{\rm t})\xi_2(s_{\rm t})$.

Note that to calculate $\xi_2^{\mathcal{AP}\ \rm template}$ (equation A5) we need to calculate $\mathcal{L}_2(\mu_{\rm f})$, where for the $\xi_{\Delta\mu}$ (equation A4) this is not needed. We test our algorithm by applying it on mock catalogues in which we assume an incorrect fiducial cosmology, and apply the above algorithm and obtain the true $1/H$ and $D_{\rm A}$ values.

In this method, we make two main assumptions. First, the AP shifting is based on a template that consists of multipoles $\ell = 0, 2$. This template can be easily expanded to higher orders of ℓ, although at scales of interest $\ell \geq 4$ components should be fairly weak. Secondly, we assume the plane-parallel approximation for each pair. Wagner et al. (2008) show that light coning yields minimal effects at $z = 1, 3$, as do Kazin et al. (2012) at $z = 0.35$.

APPENDIX B: LINEAR VERSUS NON-LINEAR AP EFFECT

Throughout this analysis, we apply the non-linear AP correction as described in Appendix A. In this section, we investigate differences with the linear AP effect as used in Xu et al. (2013). This linear approach was introduced in Padmanabhan & White (2008) in the $P(k)$ formulation, and analysed in ξ in Kazin et al. (2012). However, as pointed out by Padmanabhan & White (2008), this linear approach breaks down when $|\epsilon| > 2$ per cent, which is clearly the case in the DR9-CMASS for a large part of the 95 per cent CL region.

The linear AP correction, when applied on the clustering multipoles, is as follows.

$$\xi_0(s_{\rm t}) = \xi_0(\alpha s_{\rm f}) + \epsilon\left(\frac{2}{5}\frac{{\rm d}\xi_2(x)}{{\rm d}\ln(x)}\bigg|_{x=\alpha s_{\rm f}} + \frac{6}{5}\xi_2(\alpha s_{\rm f})\right), \quad \text{(B1)}$$

$$\xi_2(s_{\rm t}) = \left(1+\frac{6}{7}\epsilon\right)\xi_2(\alpha s_{\rm f}) + \frac{4}{7}\epsilon\frac{d\xi_2(x)}{d\ln(x)}\bigg|_{x=\alpha s_{\rm f}} + 2\epsilon\frac{{\rm d}\xi_0(x)}{{\rm d}\ln(x)}\bigg|_{x=\alpha s_{\rm f}}. \quad \text{(B2)}$$

Here, we neglect terms of the order of $\mathcal{O}(\epsilon^2)$, as well as ξ_4 terms. (For a discussion of higher order terms see section 2.2.4 in Kirkby et al. 2013.)

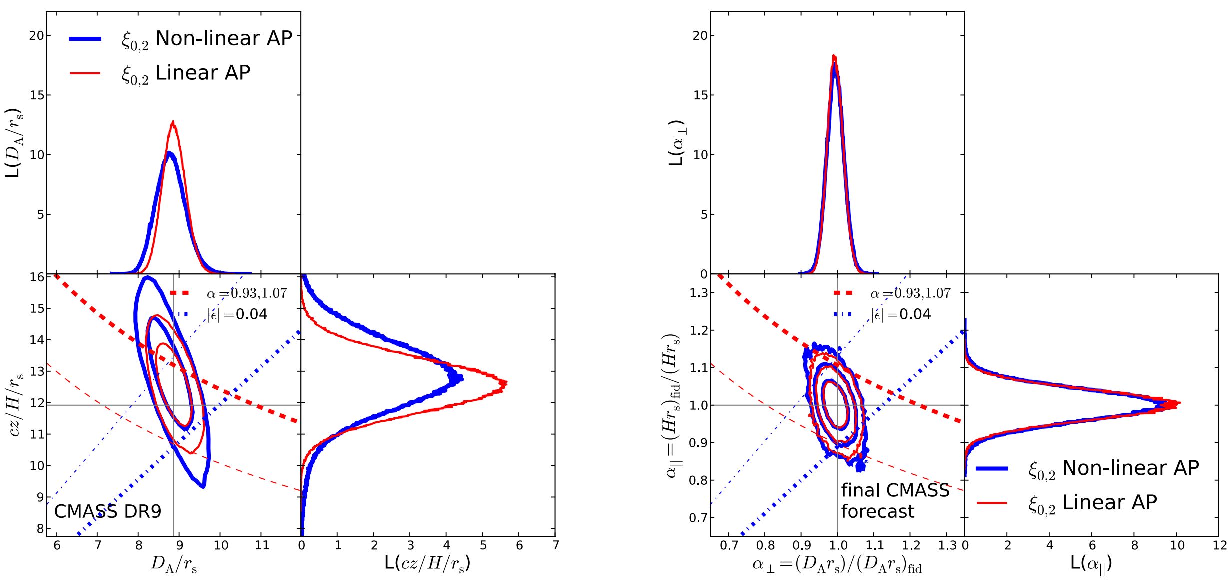

Figure B1. We use the RPT-based multipoles pre-reconstruction to test the linear (thin red) AP correction against the non-linear (thick blue) in constraining $cz/H/r_{\rm s}$ and $D_{\rm A}/r_{\rm s}$. The left-hand plot shows results for CMASS DR9 investigated here (contours are 68, 95 per cent CL regions) and the right-hand plot for projections of the final BOSS CMASS footprint (contours are 68, 95, 99.7 per cent CL regions). (As mentioned in Section 6.4, this forecast should be considered overestimated constraints as the C_{ij} used is noisier than that expected of the full CMASS volume.). To guide the eye we plot the regions of constant α and ϵ, as indicated in the legend (where the thicker line of each indicates the larger value).

The left-hand plot of Fig. B1 shows the results obtained when applying the non-linear AP (thick blue) and the linear correction (thin red) as to the CMASS-DR9 ξ. The dotted and dashed lines convey constant values of α and ϵ, respectively.

The results clearly show that the linear correction underestimates the uncertainties of $cz/H/r_{\rm s}$ and $D_{\rm A}/r_{\rm s}$ by $\sigma_H^{\rm linear}/\sigma_H^{\rm non-linear} = 7.2/9.6$ and $\sigma_{D_{\rm A}}^{\rm linear}/\sigma_{D_{\rm A}}^{\rm non-linear} = 3.2/3.9$, where $\sigma_{\rm X}^{\rm method}$ is half of the 68 per cent CL region of $\mathrm{X} = H, D_{\rm A}$. The method results agree fairly well, where ϵ is small (and regardless of α), but differ as ϵ grows. These differences should vary with the choice of the fiducial model, as well as the volume investigated.

We apply a similar comparison for a mock-mean signal (of 600 mocks) with the C_{ij} divided by 3 (as in Section 6.4) and plot the results in the right of Fig. B1. In this higher S/N test, we clearly see that the two methods agree with each other extremely well, due to the fact that ϵ is low. There is a slight underestimation of the linear approximation at the 95 per cent CL region. Note that here we test the case where the fiducial H and $D_{\rm A}$ correspond to the mock true values ($\epsilon = 0$, $\alpha = 1$), whereas if we would apply a geometric distortion of $|\epsilon| > 2$ per cent we should expect larger differences.

In conclusion, the non-linear AP correction should be applied to avoid potential estimation biases.

APPENDIX C: TESTING THE ALGORITHM ON HIGH S/N MOCKS

We test our methodology by applying it on a set of 100 mocks with higher S/N than those used in the final mock DR9 analysis. The motivation for this procedure is to separate between potential systematics and effects due to weak baryonic acoustic feature signals.

The higher S/N mocks, called 'stacked mocks', are built by stacking the 600 PTHalo DR9-volume mocks by groups of six, providing us with one hundred realizations. For purposes of this analysis, we divide the DR9 C_{ij} (see Section 5.1.1) by a factor of 6.

Fig. C1 shows distributions of $(\alpha_{||}-\langle\alpha_{||}\rangle)/\sigma_{\alpha_{||}}$ and $(\alpha_{\perp}-\langle\alpha_{\perp}\rangle)/\sigma_{\alpha_{\perp}}$ for the stacked mocks (top) and the DR9 mocks (bottom) both pre- (left) and post-reconstruction (right). The quoted p-values are obtained when performing the standard KS test between the distributions and a Gaussian one.

We find that the stacked mock results yield various Gaussian (or symmetric) attributes not found in the DR9 mock results. First, in the stacked mocks the means of the MCMC propositions are similar to the mode values, the standard deviations of the MCMC propositions are similar to half of the 68 per cent CL region and they yield low skewness values of the marginalized 1D likelihood distributions. As discussed in Section 6.2 in the DR9-volume mocks

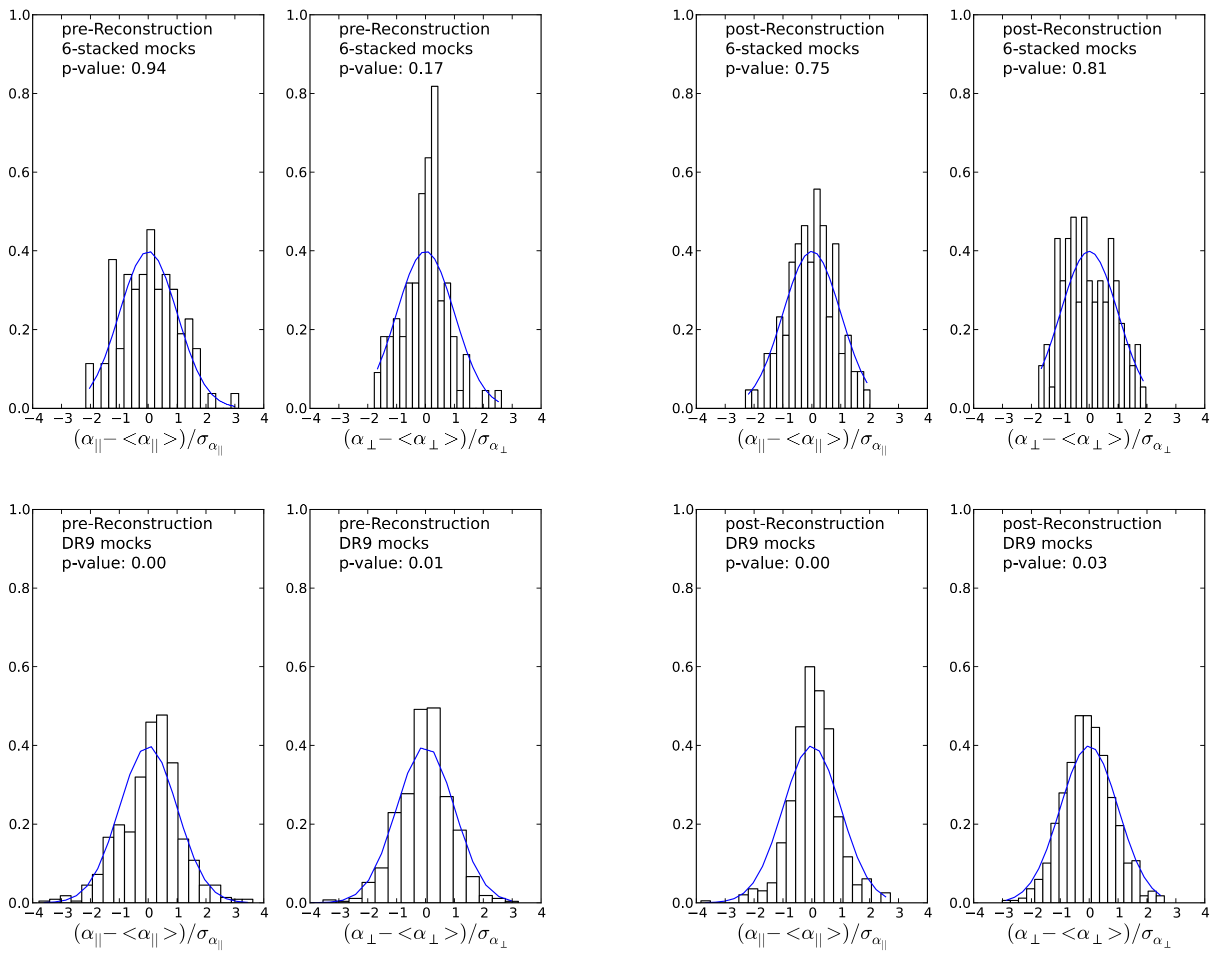

Figure C1. $(\alpha_{||}-\langle\alpha_{||}\rangle)/\sigma_{\alpha_{||}}$ results (and similar for $\alpha_{\perp}$) of 100 six-stacked mocks (top) and 600 DR9 mocks (bottom) pre- (left) and post-reconstruction (right). Results are for RPT-based clustering wedges. The p-values reflect K–S tests when comparing to a Gaussian distribution (blue lines). The p-values vary by template (RPT-based, dewiggled) and ξ statistic (clustering wedges, multipoles) used. The stacked mocks yield p-values between 20 and 95 per cent, where the DR9 mocks results have negligible p-values.

Table C1. High S/N (ix stacked) mock results.

ξ (No. of realizations)	$\alpha_{\|\|}{}^{a}$	$\Delta\alpha_{\|\|}/\alpha_{\|\|}{}^{b}$	$\alpha_{\perp}{}^{a}$	$\Delta\alpha_{\perp}/\alpha_{\perp}{}^{b}$
RPT-based wedges pre-rec (100)	1.002 ± 0.033	0.031 ± 0.006	0.996 ± 0.013	0.017 ± 0.002
RPT-based multipoles pre-rec (100)	1.002 ± 0.033	0.030 ± 0.004	0.994 ± 0.013	0.016 ± 0.001
RPT-based wedges post-rec (100)	1.005 ± 0.018	0.021 ± 0.003	0.996 ± 0.010	0.012 ± 0.002
RPT-based multipoles post-rec (100)	1.003 ± 0.016	0.022 ± 0.002	0.997 ± 0.010	0.012 ± 0.001
Dewiggled wedges pre-rec (100)	1.014 ± 0.034	0.032 ± 0.006	1.003 ± 0.014	0.017 ± 0.002
Dewiggled multipoles pre-rec (100)	1.009 ± 0.032	0.029 ± 0.004	1.003 ± 0.013	0.016 ± 0.001
Dewiggled wedges post-rec (100)	1.008 ± 0.019	0.020 ± 0.003	1.000 ± 0.011	0.012 ± 0.002
Dewiggled multipoles post-rec (100)	1.007 ± 0.014	0.017 ± 0.001	1.001 ± 0.009	0.010 ± 0.001

[a]The $\alpha_{||}$ and $\alpha_{\perp}$ columns show the median and rms of the modes.
[b]The $\Delta\alpha_{||}/\alpha_{||}$ and $\Delta\alpha_{\perp}/\alpha_{\perp}$ columns show the median and rms of the fractional uncertainties.

we find large skewness causing differences in these statistics. Using the DR9 mocks, we find that the modes and half the 68 per cent CL regions are more reliable, as they are better defined.

One of the most important Gaussian-like features found in the stacked-mock $\alpha_{||}$, $\alpha_{\perp}$ results is that the scatter in the modes is similar to the mean of the uncertainties. This is not the case for the DR9-volume mocks, probably due to weak anisotropic baryonic acoustic feature detections.

Finally, the stacked-mock results (modes and uncertainties) are similar to those yielded when applying the same C^{-1}_{ij} on the mock-mean signal (i.e. the mean signal of all 600 mocks). We find this to be true for all eight combinations investigated: clustering wedges, multipoles; RPT-based, dewiggled templates; pre-, post-reconstruction. All results are presented in Table C1.

C1 RPT-based versus dewiggled templates

As for preference of template (RPT-based versus dewiggled) for constraining $\alpha_{||}$ and $\alpha_{\perp}$, when using the stacked mocks we find strong cross-correlation coefficients of $r \sim 0.9{-}1$ in both modes and uncertainties. This comparison shows no difference in uncertainties. The only oddity we find is that the dewiggled pre-reconstruction wedges and multipoles yield median (mean) biases of 1.4, 0.9 per cent (0.9, 1.0 per cent) in $\alpha_{||}$ modes, respectively, which is reduced post-reconstruction to 0.8, 0.7 per cent (0.7 per cent). These $\alpha_{||}$ biases, when using the dewiggled model, do not appear when applied to the DR9 mocks. In those mocks, we find that the pre-reconstruction dewiggled model yields a bias of ∼1 per cent on determining $\alpha_{\perp}$.

In all four RPT-based cases (wedges, multipoles; pre-, post-reconstruction), the mean biases of $\alpha_{||}$ $\alpha_{\perp}$ are ≤0.5 per cent. Sánchez et al. (2008) thoroughly analyse differences between RPT-based and dewiggled ξ_0 and report that, when using the latter, one should expect systematic shifts in α due to the lack of a k-mode coupling term. In Section 5.2.2 we demonstrate that the post-reconstruction mocks do not prefer a template with $A_{\rm MC} = 0$, and hence suggest that templates require a mode coupling term.

For all the reasons above our choice of preference is the RPT-based template.

C2 Clustering wedges versus multipoles

The stacked mocks show no significant difference regarding the constraining power of $\xi_{||,\perp}$ and $\xi_{0,2}$ on $\alpha_{||}$ or $\alpha_{\perp}$; post-reconstruction RPT-based yields sub 0.1 per cent differences. The cross-correlation between the uncertainties of $\alpha_{||}$ are found to be $r \sim 0.6, 0.7$ (dewiggled, RPT-based), and 0.88, 0.83 for $\alpha_{\perp}$. The pre-reconstruction templates yield similar results.

We then ask if multipoles and wedges yield similar mode results. The post-reconstruction stacked mocks indicate $r \sim 0.80$ for $\alpha_{||}$ and $r \sim 0.85$ for $\alpha_{\perp}$ in both RPT-based and dewiggled templates. Pre-reconstruction results yield similar correlations.

For a visual of the results of the three-stacked mocks, please refer to the bottom plot of Fig. 14, which is described in Section 6.4.

C3 Improvement due to reconstruction

According to the stacked mock $\xi_{||,\perp}$ (and hence also $\xi_{0,2}$), we find that the uncertainty of $\alpha_{||}$ improves by 32 per cent and that for $\alpha_{\perp}$ by 30 per cent.

The stacked mocks show that the $\alpha_{||}$ modes should have a moderate correlation of $r \sim 0.5{-}0.55$ and $\alpha_{\perp}$ of 0.5−0.6. For a visual of results from the three-stacked mocks, please refer to the top plot of Fig. 14, which is described in Section 6.4.

Another value of interest is the cross-correlation between $\alpha_{||}$ and $\alpha_{\perp}$. With the stacked mocks we find this correlation to be of the order of $r \sim -0.55$ pre-reconstruction and $r \sim -0.35$ post-reconstruction. Also we find no correlation between α and ϵ modes, as expected.

This paper has been typeset from a TEX/LATEX file prepared by the author.